

Contents

1	Introduction	2
1.1	Transition edge sensors	2
1.1.1	Small signal model	4
1.1.2	Large signals	6
1.1.3	Detector metrics	8
1.2	Field programmable gate arrays	9
2	Processor design	12
2.1	Motivation	12
2.1.1	The GHZ game	12
2.1.2	Elements of reality	15
2.1.3	EPR + Bohm (EPRB) and Bell's theorem	17
2.1.4	Quantum correlations	20
2.2	Design goals	21
2.3	System overview	22
2.3.1	The multi-channel analyser (MCA)	25
3	Preliminary testing and analysis	27
3.1	Test apparatus	27
3.2	Preliminary performance analysis	29
3.2.1	Data acquisition	29
3.2.2	Dark noise	31
3.2.3	Statistical modeling	32
4	Discussion and conclusions	41
4.1	Discussion	41
4.2	Conclusions	44

Chapter 1

Introduction

1.1 Transition edge sensors

Transition Edge Sensors (TESs) are sensitive thermometers that utilise the sharp change in resistance with respect to temperature in a metal during the transition between the superconducting and normal states. The unprecedented sensitivity of transition edge sensors (TESs) has been a boon in the implementation of low temperature thermal detectors, specifically bolometers and calorimeters.

These types of detector consist of three components; an absorber of particles or incoming radiation; a thermometer, well coupled to the absorber to measure the change in internal energy from absorption events; and a weak coupling between the absorber and a cold bath to remove heat generated during detection and return it to a quiescent state (Figure 1.1). When such a detector measures power it is generally called a bolometer and when measuring energy a calorimeter. Though these terms are often used interchangeably, I'll stick to the term calorimeter since our use case is measuring photon energy.

TES based calorimeters were pioneered in Blas Cabrera's group at Stanford in the 1990's. Development was mainly aimed at astronomical use and designed to detect higher energy particles with a particular interest in detectors for the Cold Dark Mater Survey. These detectors had a separate absorber with large enough heat capacity to handle the high energies and often employed quasi-particle traps to capture athermal phonons before they thermalised. A TES was used as the thermometer that reads the internal energy change of the absorber or trap due to a particle absorption. Tungsten transition edge sensors (W-TESs) were developed for this purpose and later refined by Sae Woo Nam and his group at National Institute of Standards and Technology (NIST) Boulder to work at near-IR and optical photon energies. Tungsten was a natural choice; its phonons and electrons decouple at low temperatures providing a weak cooling link; and its superconducting transition temperature can be tuned. Tuning the transition temperature simplifies cryogenic requirements while limiting thermal noise and providing the energy resolution required to resolve near-IR photons. Tungsten has two crystal phases— α and β —by careful control of the sputtering conditions when depositing the Tungsten film the relative

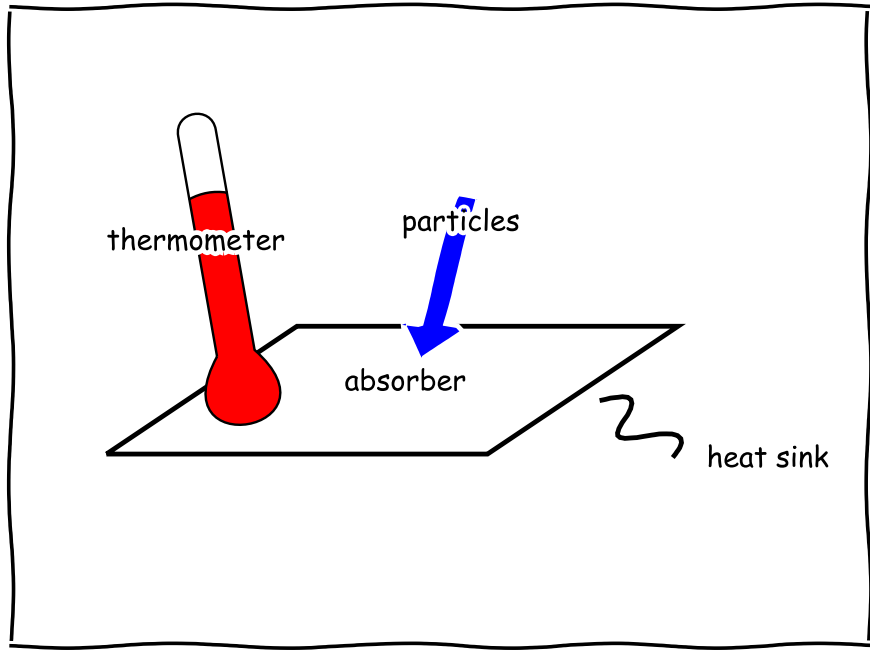


Figure 1.1: A calorimeter measures particle energy via a change in temperature. Calorimeters can be divided into 3 subsystems; an absorber for incoming particles; a thermometer to measure the absorbers internal energy change due to an absorption; and a weak link to a heat sink to cool the absorber after a detection while allowing the thermometer time to make the measurement.

proportion of the phases can be controlled altering the superconducting transition temperature [LRN⁺⁰⁵].

In the elegantly simple optical W-TES designed and fabricated by our collaborators at NIST [LCP⁺¹⁰][LMN08] all three calorimeter roles are played out in a thin film of tungsten and the W-TES thermometer *is* the calorimeter. Tungsten's electron gas acts as both absorber and thermometer while it's anomalously weak low temperature electron-phonon coupling provides the cooling link to the crystal lattice acting as the cold bath. I'll drop the term TES based calorimeter and the acronym W-TES and simply use the acronym TESs or the word sensor to refer to these exquisite NIST optical calorimeters. In operation the package of fiber coupled[MLC⁺¹¹] TESs is placed in an adiabatic demagnetisation refrigerator (ADR) and cooled to a bath temperature (T_b) $\sim 100\text{ mK}$ well below the sensors superconducting transition temperature (T_c) $\sim 150\text{ mK}$. The sensor is then biased to an operating point in the transition region between the superconducting and normal metal states using the circuit in Figure 1.2(a).

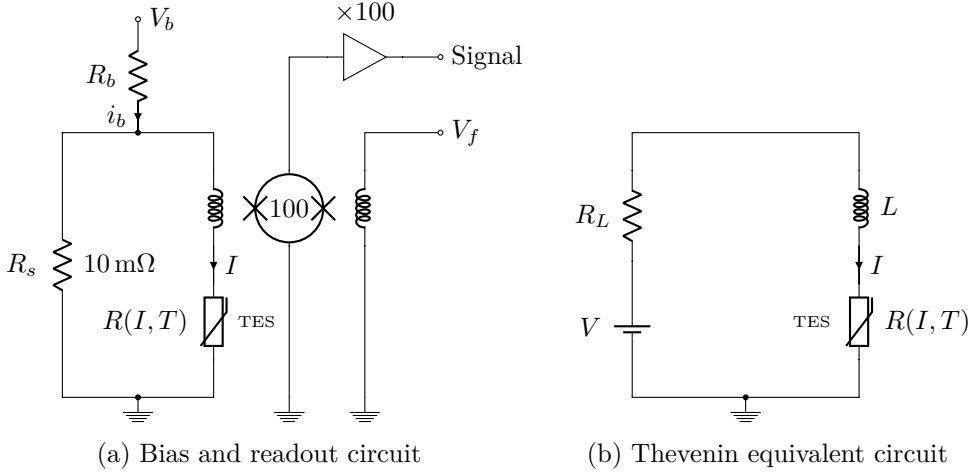


Figure 1.2: (a) Biasing and readout circuit. The TES is in parallel with a small shunt resistance (R_s) forming a divider for the bias current ($i_b \sim V_b/R_b$ as $R_b \gg R_s$). The sensor current (I) is inductively coupled to an array of DC superconducting interference devices (SQUIDS) which transduce I to a voltage signal which is further amplified at room temperature. Voltage V_f sets the operating point on the SQUID voltage-flux response to maximise transduction gain while V_b biases the sensor at an operating point (I_0, T_0) in the phase transition between the superconducting and normal metal states (see Figure 1.3).

(b) Thevenin equivalent of the bias circuit used in TES modeling, $R_L = R_s R_b / (R_s + R_b)$, $V = V_b R_s / (R_s + R_b)$ and L the inductance coupling to the SQUID.

1.1.1 Small signal model

In the simplest picture of a calorimeter the absorber is characterised by its heat capacity C and its weak link to the bath at temperature T_b by thermal conductivity G , instantaneous absorption of energy E raises the absorbers temperature by $\Delta T = E/C$ which relaxes back to T_b with a natural thermal time constant $\tau = C/G$.

A complete picture sees the TES system as coupled electrical and thermal circuits which can be described by two differential equations in the two state variables, current (I) and temperature (T),

$$L \frac{dI}{dt} = V - I(R_L + R(I, T)) \quad (1.1)$$

$$C(T) \frac{dT}{dt} = \underbrace{I^2 R(I, T)}_{\text{Joule heating}} - \underbrace{K(T^n - T_b^n)}_{\text{cooling power}} + \underbrace{E \delta(t - t')}_{\text{signal power}} \quad (1.2)$$

. The electrical equation (Equation 1.1) describes the Thevenin equivalent of the calorimeter biasing circuit (Figure 1.2b) equating the voltage across the inductor L with the voltage across the rest of the circuit, $R(I, T)$ is the current and temperature dependant TES resistance. Similarly, Equation 1.2 describes the thermal circuit equating energy change to power in and out of the calorimeter, cooling to the bath is described by a power law with constant K and exponent n and the signal power term represents deposition of energy E at time t' under

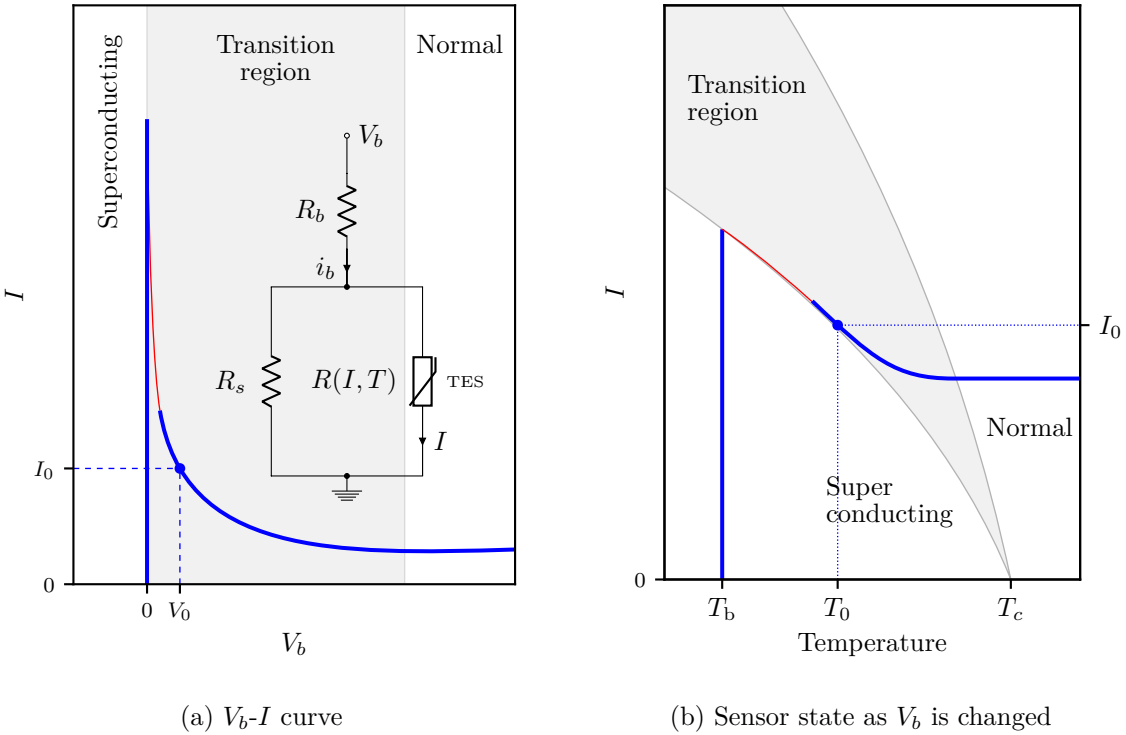


Figure 1.3: Sensor trajectory as bias voltage is changed: At 0 V bias the sensor is at the bath temperature (T_b) well below its superconducting transition temperature (T_c) and has 0 resistance. When the bias voltage (V_b) is increased above 0 V the sensor current (I) rapidly increases until it reaches the critical value and the sensor enters the transition between the superconducting and normal phases. In the transition the sensor state can be considered a mixture of the superconducting and normal phases with the proportion of normal phase and resistance increasing with temperature. Current flowing through the non-zero resistance dissipates power increasing the sensors temperature. For any fixed bias voltage the bias current (i_b) is also fixed, variation in the sensors resistance varies the sensor current I by changing the division of i_b between the sensor and the shunt resistance R_s . As I changes so does the power dissipated which in turn changes the sensor temperature. This feedback between current and temperature is known as electro-thermal feedback (ETF). For a fixed v_b , ETF acts to stabilise the TES at some equilibrium point int the phase diagram. The blue line indicates the trajectory of this equilibrium point through the phase diagram as v_b is increased. The equilibrium temperature increases and the equilibrium current decreases as v_b increases until the sensor leaves the transition and enters the normal resistance region. The thin red segments in the figures are regions where the no stable equilibrium exists. The bias voltage is adjusted to find the equilibrium point (I_0, T_0) that achieves the highest gain for converting temperature change into a current change.

the assumption the event causes an instantaneous change in temperature of the absorber-thermometer system.

The cross terms in the equations describe a feedback interaction between the electrical and thermal circuits known as ETF [NCC⁺99][Irw95]. The sensor/thermometer is characterised by its local logarithmic sensitivity, defined as $\alpha \equiv \frac{d \ln R}{d \ln T}|_{V_q}$ by some authors and by a constant current derivative $\alpha_I \equiv \frac{\partial \ln R}{\partial \ln T}|_{I_q}$ and a constant temperature derivative $\beta_I \equiv \frac{\partial \ln R}{\partial \ln T}|_{T_q}$ by others. These logarithmic sensitivity terms describe the shape of the transition. In the case of W-TES α is positive which when combined with voltage biasing leads to negative feedback between current and temperature. A rise in temperature increases TES resistance which reduces the current I flowing the TES arm of the circuit (Figure 1.2a) reducing the power dissipated and cooling the sensor. The reverse is true for falls in temperature. Negative ETF stabilises the TES in the transition region at a quiescent equilibrium point and reduces the relaxation time below that given by the natural time constant τ . Negative ETF acts much the same way as negative feedback acts in amplifiers to linearise and stabilise the output. The NIST W-TES operate with extreme negative ETF and the energy deposited by a photon is removed by the reduction in Joule heating while cooling power to the bath is essentially constant. In the extreme ETF regime detection energy is proportional to integral of the current pulse.

Small signal models are well developed and illuminating, they are constructed by linearising the coupled differential equations about the quiescent operating point (I_0, T_0) and expanding to first order [IH05][Lin00][McC05] following [IH05] which expands the analysis in [Lin00] and leaving the detail in the references, the linearised equations 1.1 and 1.2 can be put in a matrix form

$$\frac{d}{dt} \begin{pmatrix} \delta I \\ \delta T \end{pmatrix} = \begin{pmatrix} \frac{1}{\tau_{el}} & K_1 \\ K_2 & \frac{1}{\tau_I} \end{pmatrix} \begin{pmatrix} \delta I \\ \delta T \end{pmatrix} + \begin{pmatrix} \frac{\delta V}{L} \\ \frac{\delta P}{C} \end{pmatrix}, \quad (1.3)$$

where $\delta I \equiv I - I_0$, $\delta T \equiv T - T_0$, $\delta V \equiv V - V_0$, $\delta P \equiv P - P_0$, P being the signal power and $P_0 = I_0^2 R(I_0, T_0)$. The two time constants τ_{el} and τ_I characterise the the decay of I to I_0 in the bias circuit and the decay of T to T_0 under a constant current. The two lumped constants K_1 and K_2 are dependant on the operating point and physical parameters (see [IH05] Equation 19).

Homogeneous solutions, $\delta V = \delta P = 0$, are of the form

$$\begin{pmatrix} \delta I \\ \delta T \end{pmatrix} = A_+ e^{\lambda_+ t} \mathbf{v}_+ + A_- e^{\lambda_- t} \mathbf{v}_-, \quad (1.4)$$

where λ_{\pm} and \mathbf{v}_{\pm} are the eigenvalues and eigenvectors of the the matrix in Equation 1.3 while A_{\pm} are unitless constants. The eigenvalues yield the rise and fall time constants for the current pulse $\tau_{\pm} = 1/\lambda_{\pm}$ and the eigenvectors give the directions for the rise and decay in the sensors phase diagram (see Figure 1.4a).

1.1.2 Large signals

As the detection energy increases the TES response is no longer described by the linear small signal model. The response becomes more and more non-linear as detection energy increases

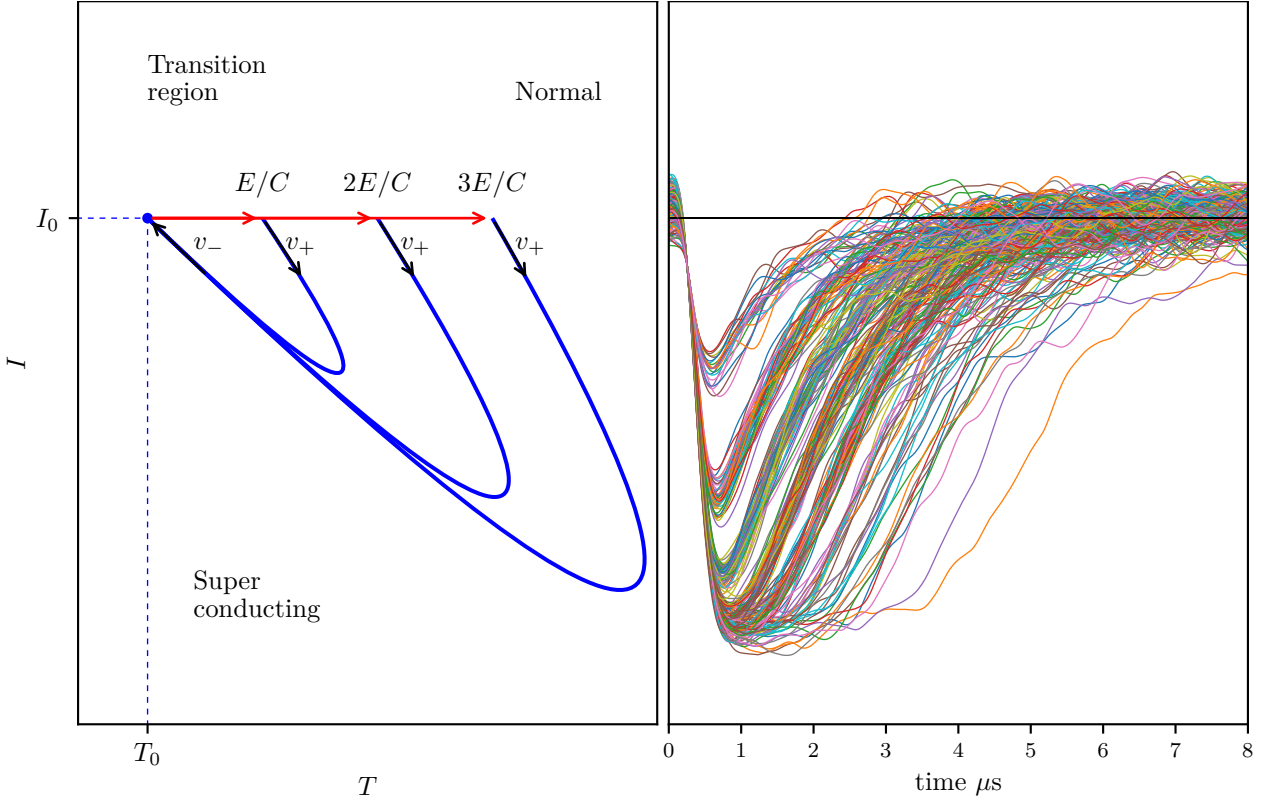


Figure 1.4: Left pane: A qualitative illustration of the sensor state trajectory during photon detection as described by the small signal model. The eigenvectors (\mathbf{v}_{\pm}) of the matrix in Equation 1.3 indicate the directions of the the rise (\mathbf{v}_{+}) and fall (\mathbf{v}_{-}) of the detection pulse while the eigenvalues are the inverse of the rise and fall time constants. The small signal model assumes that absorption of energy E instantaneously raises the sensor temperature by E/C where C is the sensors heat capacity.

Right pane: TES detection pulses after processing by hardware simulation. The optical input is a ~ 830 nm 100 kHz pulse train with average photon number ~ 2 . The pulses are inverted to match the direction of the sensor current changes in the left pane. The collection of pulses are randomly coloured and illustrate the sensor’s response in different energy regimes. For 830 nm photons these are roughly; (1-2 photons) the linear regime where the small signal model holds; (2-4 photons) the non-linear regime where scaling in of the TES response with photon number is non-linear; (5 + photons) saturation, the TES has been driven out of the transition, its resistance is no longer dependent on the current and all the enhancements to thermometry and cooling that the transition region provides no longer apply. While saturated the TES still acts like a normal cold metal calorimeter with energy information encoded in the time required to cool back into the transition. The integral of the pulse still encodes energy past saturation albeit with reduced resolution.

until the sensor is driven out of the transition into the normal regime and is saturated.

Although the superconducting transition is well understood theoretically the precise nature of TES resistance $R(I, T)$ in real devices outside the realm of the small signal model is not.

None the less several techniques have been explored for improving analysis of TES signals in the non-linear and early saturation regimes[BAB⁺15][FFCM⁺00] [LGM⁺14].

1.1.3 Detector metrics

As photon detectors TESs outperform competing technologies in two detector metrics:

Detection efficiency TESs have an near unity intrinsic detection efficiency for photons that reach the sensor and a system detection efficiency above 95%.

Dark counts TESs have zero intrinsic dark counts. All output pulses originate from a real detection, never from some spontaneous event in the detector or low temperature readout electronics. There are of course background counts from stray light and the high energy tail of the blackbody spectrum.

. A TES is also one of the few technologies that provide *true* number resolution through the ability to resolve energy and are unique in combining number resolution, high detection efficiency and low dark counts. I use the phrase “true number resolution” here to distinguish between the use of “number resolution” by technologies using multiple non-number resolving detectors to provide pseudo-number resolution.

TESs underperform in the remaining two detector metrics:

Timing jitter The uncertainty in the photon arrival time extracted from a TESs detection pulse is comparatively large. TES jitter can be improved by reducing inductance in the readout circuit (Figure 1.2a) which is dominated by the SQUID input coil. Reducing the inductance decreases the rise time constant (Equation 1.4) and increases the rising slope of the detection pulse. When timing is based on a threshold crossing the jitter is related to the TES noise-dominated by Johnson noise and thermal fluctuation across the link between absorber and bath- and the slope of the signal at the threshold. This improvement is demonstrated in [LLCT⁺13] where the use of low input inductance SQUID amplifiers [DAB⁺07] reduces the jitter to 4.1 ns at 1550 nm and 2.3 ns at 775 nm. The downside is the coax cabling required adds heat load to the cryostat and complicates wiring limiting the number of detectors that can be supported in a cryostat. Limited availability of the low inductance SQUIDs has also limited deployment of these low jitter TES systems. For the sensors in our lab with relatively high inductance SQUIDs and twisted pair wiring the jitter is ~ 80 ns full width half maximum.

Recovery time Also called dead-time. TESs have no intrinsic dead time and continuously detect but the long relaxation time leads to *pile-up* of detection pulses when another photon is detected before the TES has fully recovered from the previous detection. Pile-up complicates the extraction of the detection information and limits the usable TES detection rate. The recovery time can also be improved, [CLFN11] reports a four fold

reduction in the fall time constant without significant loss of energy resolution. This is achieved by increasing the coupling between the TES and the cold bath using normal metal heatsinks.

I'll add an informal metric¹, ease of use. Compared to the current workhorse detector for quantum information experiments, the avalanche photo-diode, TESs are extremely difficult to use. To count photons with an avalanche photo-diode it simply needs to be powered up and connected to something that can count standard logic pulses. To count photons with a TES you must cool it to 100 mK then you must deal with its analogue output. Ease of use and accessibility to these remarkable sensors was a factor motivating this project.

Improvements to TESs will ultimately hit limits imposed by the underlying physics [IHWM98] and engineering constraints for producing a stable device. It would appear unlikely that TESs will ever become a workhorse detector for quantum information which mostly demands efficient and rapid counting of single photons. The leading candidate technology for this role is based on superconducting nanowires which offer; high detection efficiency, not yet at levels offered by a TES but still improving; very low jitter; low recovery time and counting rates in hundreds of millions of counts per second; architectures that can provide pseudo-number resolution; and have higher operating temperatures requiring less expensive and more convenient continuous cycle cryogenics. See chapters 1 and 2 of [Ens05] for a review of both technologies in the context of quantum optics and information. Nonetheless, TESs find use in quantum information experiments that exploit the sensors unique strengths. The unrivaled detection efficiency of TESs has allowed violation of quantum steering and Bell inequalities without assuming fair sampling. Number resolution, though not generally required in quantum information, allows direct examination of the consequences of assuming a source is emitting single photons and opens up higher dimensional spaces to experiments.

1.2 Field programmable gate arrays

Experimental experience with TESs gained during our quantum steering project[SGdA⁺12] highlighted the usefulness of realtime detection information, see section 2.1 for more detail. The methods used by others to extract time and energy information from the detection pulses involve digitisation of the TES output then processing with software. While software based approaches allow arbitrarily complex processing to achieve low uncertainty for the energy estimates, they are difficult to scale past a few TES channels while still providing realtime number resolved coincidence counts. I decided to explore *hardware* processing of the signal and the subject of this thesis is a library of digital circuits designed specifically for processing TES detection pulses. The circuit library is used to create a prototype hardware signal processor which focuses on producing a digital stream of event packets with minimal latency between a detection and the

¹A metric of particular importance to PhD students.

event packet being available. Each detection pulse produces an event packet containing pulse measurements and a timestamp. The downside of using hardware is that processing complexity is constrained to processes implementable as circuits.

The modern approach to prototyping digital hardware is to use field programmable gate arrays (FPGAs) to implement circuits described in a hardware definition language (HDL). HDL descriptions can be confused with a program written for a general purpose computer but any similarity is superficial. Though HDLs are general languages capable of universal computation only a subset of statements in the language are *physical* and can be realised as a circuit. A number HDLs exist and the two most widely used emerged in the 1980's. I choose to use VHDL a language created by the United States department of defence to address the problems encountered while re-procuring hardware based on obsolete technologies. VHDL was designed to document and describe all components of a system so that new circuits could be constructed that function identically to obsolete parts. Consequently, VHDL has wide descriptive capabilities making it quite verbose but offers higher levels of abstraction than the alternative HDL from the period, Verilog.

Since the 1980's other HDLs have emerged, most notably SystemC and System-Verilog, offering levels of abstraction approaching that of general computer languages which potentially makes complicated circuits easier to verify, modify, maintain and reuse. Unfortunately tools were not available for these languages at the beginning of this project. Recent developments include tools that convert algorithms written in C into HDL circuit descriptions which may lower the entry barrier for those wanting to add to the library.

Back in the day, digital design and prototyping involved discrete components and a “breadboard” which allowed the connections between components to be adjusted to easily change the circuit. FPGAs are the evolution of this, they contain large array of components or *resources* embedded in a reconfigurable routing matrix allowing the connections between resources to be changed to create different circuits. FPGA resources can be divided into two categories; *Fabric* resources are ubiquitous and arranged in cells containing fundamental low level digital components, the fabric cell array covers the majority of the FPGA chip die; *Hard cores* are dedicated silicon performing a specific function, effectively internal chips. Fabric resources are general and can be used to construct *any* circuit but the many connections between the low level components required to implement a complex circuit in fabric limit the rate at which it can be clocked. Hard cores provide dedicated functionality for example, random access memory (RAM), transceivers or multiply and accumulate block for use in digital signal processing (DSP) and run at speeds comparable to discrete chips.

Digital circuits are built from two types of logic; *combinatorial* logic elements have outputs that change whenever any input changes, for example a logic gate; *sequential* logic elements have outputs that change synchronously with a *clock* edge, the canonical example being a register or flip-flop. In order to function reliably and deterministically the inputs to sequential elements must not change in a window around clock edge defined by the *setup* and *hold* time,

see Figure 1.5. When all sequential elements in a circuit satisfy the setup and hold requirements the circuit is said to *meet* timing.

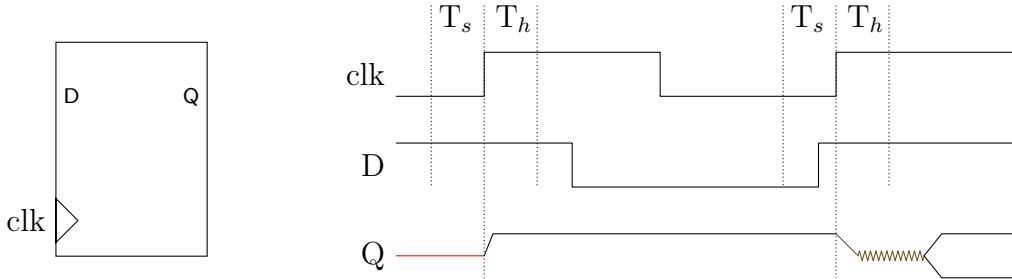


Figure 1.5: A register, also known as a D-type flip-flop, is a sequential logic element. The output (Q) is the value of the input (D) sampled at a rising transition of the clock signal (clk). To function correctly the input must be stable during the aperture that extends from the setup time (T_s) before the clock transition to the hold time (T_h) after it. If this timing constraint is violated the register can enter a metastable state which eventually decays to either $Q = H$ or $Q = L$ in a non-deterministic manner.

The HDL circuit description is processed by a toolchain which proceeds in three phases. *synthesis* infers generic circuit elements from the HDL statements and creates a *netlist* describing the circuit. *Mapping* takes the netlist and replaces the generic elements with the specific resources available in the particular FPGA. *Place and route* takes the mapped netlist and places each mapped element in the FPGAs resource array in such a way that the FPGAs routing matrix can realise all netlist connections. This placement is then optimised over a number of passes with the goal of ensuring the design meets its timing constraints. The placed and routed design is then converted to a bitstream that can be uploaded to the FPGA to realise the design.

I used a Xilinx 6 series FPGA (Virtex6) to implement the processor which uses a toolchain called ISE which was created at the time Xilinx was producing 3 series devices. Since I began the project Xilinx released 7 series devices and a new toolchain called Vivado. Unfortunately Vivado is not backwardly compatible and only works with 7 series devices and above. Xilinx make excellent FPGA hardware but the software leaves a lot to be desired, particularly ISE. Vivado appears to be a vastly better tool-chain. The processor is stuck at the compatibility break and needs to be ported from ISE to Vivado. ISE can only meet timing for the design when two processing channels are instantiated. Four are possible when specific placement constraints are added for the place and route optimisation but any design changes require new constraints to be found. Vivado appears to have better optimisation routines and the Virtex7 has faster routing and more resources. When the design is ported to Vivado I expect 8 channels will meet timing routinely and without extra constraints.

Chapter 2

Processor design

2.1 Motivation

My first experience using TESs in a quantum information experiment was working on a project that violated a *quantum steering* inequality while closing the detection loophole [SGdA⁺12]. Steering is the ability to remotely prepare part of a multipartite state into different ensembles of states by performing different measurements on another part. Steering requires and serves to certify *entanglement* which is a strong *non-classical correlation* between subsystems of a multipartite quantum state.

2.1.1 The GHZ game

Non-classical correlation is perhaps best described by considering a cooperative three player game called the GHZ game. During play the players—Alice, Bill and Clarisse—are isolated in separate laboratories and communication between labs is *physically impossible*. Each lab contains a blank display that will show a symbol—either X or Y—during play as well as two mutually exclusive buttons labeled +1 and -1 that each player uses to respond to the symbol. Before being isolated the players are told the rules of the game and are free to communicate and share information and resources in an attempt to devise a foolproof strategy. Here I use the term foolproof to describe strategies that *always* win. The two rules are; when a symbol is displayed each player must respond by pressing a button; and either the symbol X will be displayed in *all* labs, or X will be displayed in exactly one lab while Y is displayed in the others. The players win the game if the product of their responses is +1 when all lab displays show X and -1 otherwise.

The possible games and the winning response products can be represented as a set of four

equations

$$\begin{aligned} r_X^A r_X^B r_X^C &= +1 \\ r_X^A r_Y^B r_Y^C &= -1 \\ r_Y^A r_X^B r_Y^C &= -1 \\ r_Y^A r_Y^B r_X^C &= -1. \end{aligned} \tag{2.1}$$

The LHS of (2.1) is the product of terms of the form r_j^i indicating the response of player $i \in \{A(\text{lice}), B(\text{ob}), C(\text{larise})\}$ to symbol $j \in \{X, Y\}$ while the RHS is the response product required to win. Multiplying the equations together reveals a contradiction,

$$\begin{aligned} \text{LHS} &= (r_X^A)^2 (r_Y^A)^2 (r_X^B)^2 (r_Y^B)^2 (r_X^C)^2 (r_Y^C)^2 = +1 \\ \text{RHS} &= +1 \times -1 \times -1 \times -1 = -1. \end{aligned} \tag{2.2}$$

This contradiction proves that no foolproof deterministic strategy exists, ie there are no foolproof strategies where the players have predetermined their responses to a symbol.

A similar argument proves that no foolproof non-deterministic strategy exists. In non-deterministic strategies each player i responds to symbol j by pressing $+1$ with probability p_j^i and pressing -1 with probability $1 - p_j^i$. Under the non-deterministic strategy the r_j^i terms on the LHS of (2.2) become expectation values $\langle r_j^i \rangle$ with values in the interval $[-1, +1]$. A similar contradiction occurs because the product of the squared expectation values must be greater than or equal to 0.

In the most general case the players share some correlated resource before being isolated in the labs. The correlations shared through the resource cannot be dependant on the symbols the players see during play as the symbols are unknown when they are able to share. Resources the players share can be described as conditions on extra shared variables which can have values Λ , letting $\rho(\lambda)$ be the probability that the variables have a particular value $\lambda \in \Lambda$ a description of *every* classical strategy allowed under the rules of the game can be constructed. Equations 2.1 become,

$$\begin{aligned} \int d\lambda \rho(\lambda) r_X^A(\lambda) r_X^B(\lambda) r_X^C(\lambda) &= +1 \\ \int d\lambda \rho(\lambda) r_X^A(\lambda) r_Y^B(\lambda) r_Y^C(\lambda) &= -1 \\ \int d\lambda \rho(\lambda) r_Y^A(\lambda) r_X^B(\lambda) r_Y^C(\lambda) &= -1 \\ \int d\lambda \rho(\lambda) r_Y^A(\lambda) r_Y^B(\lambda) r_X^C(\lambda) &= -1, \end{aligned}$$

where $r_j^i(\lambda)$ is the response of player i to symbol j when the shared variables have value λ .

Since $\rho(\lambda)$ is a probability a foolproof strategy can only exist if for some particular λ

$$\begin{aligned} r_X^A(\lambda) r_X^B(\lambda) r_X^C(\lambda) &= +1 \\ r_X^A(\lambda) r_Y^B(\lambda) r_Y^C(\lambda) &= -1 \\ r_Y^A(\lambda) r_X^B(\lambda) r_Y^C(\lambda) &= -1 \\ r_Y^A(\lambda) r_Y^B(\lambda) r_X^C(\lambda) &= -1. \end{aligned}$$

Which raises the same contradiction (2.2) proving that no strategy based on classical resources is foolproof.

When the players have access to quantum resources a foolproof strategy *is* possible. Consider the tripartite spin- $\frac{1}{2}$ entangled state $|GHZ\rangle = \frac{1}{\sqrt{2}}(|000\rangle + |111\rangle)$ where 0 (1) indicates spin up (down) in the Pauli z basis¹. If each player takes a subsystem of a $|GHZ\rangle$ state into their lab then measures it in the Pauli basis corresponding to the symbol displayed and responds with the outcome they can always win.

Consider the set of commuting observables

$$\begin{aligned} \sigma_x^A \sigma_y^B \sigma_y^C \\ \sigma_y^A \sigma_x^B \sigma_y^C \\ \sigma_y^A \sigma_y^B \sigma_x^C, \end{aligned} \tag{2.3}$$

though the x and y components of the spin of an individual particle anti-commute $\{\sigma_x^i, \sigma_y^j\} = \sigma_x^i \sigma_y^j + \sigma_y^j \sigma_x^i = 0$, the commutator of any pair in the set introduces an even number of anti-commutations which cancel out. $|GHZ\rangle$ is a *simultaneous* eigenstate with eigenvalue -1 of all three and the observables correspond to the three possible games in which only one lab displays the symbol X . The product of the individual players measurement outcomes is equivalent to the eigenvalue -1 so they always win games where only one lab displays X . Similarly the observable

$$\sigma_x^A \sigma_x^B \sigma_x^C \tag{2.4}$$

commutes with the previous three (2.3) and $|GHZ\rangle$ is simultaneously an eigenstate of all four. The eigenvalue for $\sigma_x^A \sigma_x^B \sigma_x^C$ is $+1$ so when all labs display X the product of the players responses is $+1$ and they always win.

Why is it so? The players are allowed arbitrary sharing and communication to establish arbitrary correlations between themselves yet a foolproof strategy does not exist if the resources they share are classical but does if they are quantum. The only constraints are that the sharing must be done in ignorance of what symbol each player will see as that information does not yet exist and once that information does exist it cannot be shared. Always winning the GHZ game is impossible classically—which is the standpoint of our common sense and intuition—what is it about quantum mechanics that allows a foolproof strategy? Perhaps the answer lies in questions about when and where information exists.

¹Most famously analysed by Greenberger, Horne and Zeilinger [GHSZ90]

2.1.2 Elements of reality

When using classical resources in the GHZ game the information governing player responses *exists* at the time they establish correlations between themselves then waits to be revealed once they enter the lab and see a symbol. When the the information dictating player responses exists *before* the symbol is known the contradiction in (2.2) is inevitable and it is impossible to always win the game.

Quantum mechanics introduces the notion that physical properties generally have no objective reality independent of the act of observation and the act of measuring *creates* what is measured. Uncertainty relations are understood not just as a prohibition on what is co-measurable but on what is simultaneously real. Underlying this is the generally unavoidable disturbance quantum measurement has on what is measured through quantum back-action. In general the more information is gained by measurement of a quantum system the greater the disturbance to it [Bra05][GDL⁺10].

When the players use quantum resources the information on which they base their responses does not exist when they share resources prior to entering the lab, it is brought into existence when they see the symbol and perform the corresponding measurement. The four observables (2.3-2.4) all commute and $|\text{GHZ}\rangle$ is simultaneously an eigenstate of them all. Since the corresponding eigenvalue is the product of the three measurement outcomes on the individual particles, measurement on any two particles determines the outcome of the third. The rules of game are designed to perfectly exploit this remarkable non-classical correlation in the $|\text{GHZ}\rangle$ state which assures the players always respond in a coordinated way and win. A quantum resource allows players win through what Einstein dubbed “spooky action at a distance”.

This notion that the act of measurement creates what is measured troubled Einstein. Pais, who often accompanied Einstein on his lunchtime walk home from the Institute of Advanced Study in Princeton, recalls[Pai79]

We often discussed his notions on objective reality. I recall that during one walk Einstein suddenly stopped, turned to me and asked whether I really believed that the moon exists only when I look at it. The rest of this walk was devoted to a discussion of what a physicist should mean by the term “to exist”.

Einstens position was first and most famously formalised in the 1935 Einstein, Podolsky and Rosen (EPR)[EPR35], which asks “Can Quantum-Mechanical Description of Physical Reality Be Considered Complete?”. The paper contains two assertions

- Quantum theory is incomplete.
- Incompatible observables cannot be simultaneous elements of reality.

and the authors argue that only one assertion can hold.

The EPR paper examines the interpretation of quantum state vectors through a thought experiment on a quantum system consisting of two particles moving away from each other such

that their total linear momentum is zero. In this arrangement the position and momentum of the particles are perfectly correlated. By measuring the momentum of one particle (p) the momentum of the other can be inferred from the correlation ($-p$), similarly for position. The two systems are measured when they are well separated and in such a way that no signaling between them is possible, ie information from measurement of one particle cannot influence measurement of the other.

EPR make two assumptions without directly addressing them; *locality* prohibits distant measurements of one particle disturbing what is considered “real” for the other system; and *separability* establishes each system has a separate reality in the form of an individual physical state.

In a nutshell incompleteness argument is; Spatially separate particles have individual real physical states (separability); if particles are spatially separated measuring or not measuring one particle cannot directly affect the reality of others (locality); if quantities on separate particles are strictly correlated those quantities have definite values (often called the EPR lemma). From the lemma, the system described in the paper has simultaneous definite values of both position and momentum and since these values cannot be inferred from quantum mechanical formalism the quantum mechanical description must be incomplete.

The EPR lemma is arrived at through the slippery notion of “elements of reality” which are defined in the paper by what is now known as the EPR criterion of reality:

If, without in any way disturbing a system, we can predict with certainty (i.e., with probability equal to unity) the value of a physical quantity, then there exists an element of reality corresponding to that quantity.

The reality criterion asserts that a quantity has a value that exists irregardless of whether it measured or not when we can predict the value of that quantity with certainty.

The $|GHZ\rangle$ state, which had not been analysed at the time of the EPR paper, makes it clear that the EPR criterion of reality is in direct conflict with the predictions of quantum mechanics. Measurement of $|GHZ\rangle$ using the observables in (2.3) yields results

$$\begin{aligned} r_X^A r_Y^B r_Y^C &= -1 \\ r_Y^A r_X^B r_Y^C &= -1 \\ r_Y^A r_Y^B r_X^C &= -1. \end{aligned} \tag{2.5}$$

where r_j^i is the outcome of measuring σ_j for subsystem i and the RHS is the eigenvalue of $|GHZ\rangle$ for the observable. We can predict the value of the outcome of a measurement on any of the subsystems with certainty by measuring the other two. By the EPR reality criterion each r_j^i corresponds to an element of reality and has a value that exists before it is measured. The product of the equations in (2.5) is $r_X^A r_X^B r_X^C = -1$ since $r_j^i = \pm 1$. This conflicts with a direct measurement of $\sigma_x^A \sigma_x^B \sigma_x^C$ which has result $r_X^A r_X^B r_X^C = +1$.

Einstein further developed, focused and clarified his incompleteness argument in later publications in which the concept of “elements of reality” thankfully falls by the wayside. These later publications draw directly on the the notions of separability and locality implicitly assumed in the original EPR paper to make a case for incompleteness. The arguments between the Einstein and Bohr camps over the completeness of quantum mechanics is considered the greatest philosophical debate of early quantum theory. Bohr published a refutation of the original EPR paper under the same title in the same journal. A less obfuscated and more accessible view opposing the realist perspective is found in a 1954 letter from Pauli to Born[EM]

As O. Stern said recently, one should no more rack one’s brain about the problem of whether something one cannot know anything about exists all the same, than about the ancient question of how many angels are able to sit on the point of a needle. But it seems to me that Einstein’s questions are ultimately always of this kind.

Surprisingly Pauli and Stern were wrong, brain racking by Bohm and Bell led to results that made the EPR claims experimentally testable.

2.1.3 EPR + Bohm (EPRB) and Bell’s theorem

In the late 1950’s Bohm[BA57][BA60] began considering ideas presented by EPR and developing thought experiments based on incompatible measurements of spin rather than position and momentum. Inspired by Bohm’s thought experiments Bell pioneered the work that led to the theorem that now bears his name. Bell’s Theorem is a collection of results proving that local realistic theories like the one proposed by EPR, also known as local hidden variable theories, are incompatible with quantum mechanical predictions. Different local hidden variable theories give different meanings to “local realistic”. In Bell’s 1964 paper[Bel64] the realism consisted of postulating that in addition to quantum states there exist “complete states”, or hidden variables, that determine measurement results. The paper derives an inequality that bounds the correlation that can be observed in an electron spin experiment given particular local realist assumptions. Bell’s original work has been generalised and refined and now a plethora of inequalities that bound correlation for local realist theories are collectively referred to as Bell inequalities. The Bell inequality derived by Clauser, Horne, Shimony and Holt (CHSH)[CHSH69] was applicable to photon polarisation and at the time opened the possibility of more tractable experimental realisations than provided electron spin as originally analysed by Bell.

Hidden variable models are probabilistic. Let $\rho(\lambda)$ be a probability distribution over the space of complete states Λ where $\lambda \in \Lambda$ represents a particular complete state. Two parties, Alice and Bob, are well separated and each makes measurements on one particle of an entangled pair. Each party can perform one of two measurements; Alice’s measurement operators

are $m^A \in \{A_{\pm}, A'_{\pm}\}$ with respective measurement outcomes denoted a_{\pm} and a'_{\pm} which are collectively labeled r^A ; similarly, Bobs measurement operators are $m^B \in \{B_{\pm}, B'_{\pm}\}$ with outcomes b_{\pm} and b'_{\pm} which are collectively labeled r^B . All outcomes are ± 1 . The following probabilities are assumed to be well behaved ($\forall \lambda \in \Lambda$);

$$p(r^A|m^A, m^B, r^B, \lambda) \text{ and} \quad (2.6)$$

$$p(r^B|m^A, m^B, r^A, \lambda) \quad (2.7)$$

are the probabilities of one parties outcome conditioned on the other parties outcome when the complete state is λ ; and

$$p(r^A, r^B|m^A, m^B, \lambda) \quad (2.8)$$

is the probability of the outcomes of joint measurements by both parties when the complete state is λ .

Locality results from the following assumptions; *remote outcome independence* assumes one parties outcome does not depend on the outcome of other, ie that

$$\begin{aligned} p(r^A|m^A, m^B, r^B, \lambda) &\equiv p(r^A|m^A, m^B, \lambda) \text{ and} \\ p(r^B|m^A, m^B, r^A, \lambda) &\equiv p(r^B|m^B, m^B, \lambda); \end{aligned} \quad (2.9)$$

while *remote context independence* assumes that one parties outcome does not depend on the measurement choice of the other

$$\begin{aligned} p(r^A|m^A, m^B, \lambda) &\equiv p(r^A|m^A, \lambda) \text{ and} \\ p(r^B|m^A, m^B, \lambda) &\equiv p(r^B|m^B, \lambda). \end{aligned} \quad (2.10)$$

The conjunction of these assumptions is equivalent to the factorisation condition[Jar84]

$$p(r^A, r^B|m^A, m^B, \lambda) \equiv p(r^A|m^B, \lambda) p(r^B|m^B, \lambda) \quad (2.11)$$

which is often referred to as *Bell locality*. For Einstein, locality restricts influences on the “real” physical states of spatially separated systems. For Bell, locality is focused instead on influences on the outcomes of joint measurements on separated systems.

Noting that the probability measurements m^A and m^B have outcomes r^A and r^B is

$$p(r^A, r^B|m^A, m^B) = \int d\lambda \rho(\lambda) p(r^A|m^A, \lambda) p(r^B|m^B, \lambda) \quad (2.12)$$

and defining the correlation between measurements as the expectation value of the product of their outcomes, we have

$$c(m^A, m^B) = \sum_{i,j} r_i^A r_j^B p(r_i^A, r_j^B|m^A, m^B), \quad (2.13)$$

where the sum is over all measurement outcomes. The CHSH inequality bounds a particular combination of of measurement correlations

$$S_{CHSH} = c(A, B) + c(A, B') + c(A', B) - c(A', B'). \quad (2.14)$$

S_{CHSH} can be bounded by fixing λ and examining the sum of products

$$\begin{aligned} S = \sum_{i,j} a_i p(a_i|A, \lambda) [b_j p(b_j|B, \lambda) + b'_j p(b'_j|B', \lambda)] + \\ a'_i p(a'_i|A', \lambda) [b_j p(b_j|B, \lambda) - b'_j p(b'_j|B', \lambda)]. \end{aligned} \quad (2.15)$$

Since that absolute value of the terms of the form $a_i p(a_i|A, \lambda)$ are bounded by by 1, the absolute value of each line in the sum is bounded by 2. When value of one of the square brackets is 2 the value of the other is 0 so the absolute value of the sum is bounded by 2. Multiplying (2.15) by $\rho(\lambda)$ and integrating over λ gives S_{CHSH} , so $|S_{CHSH}| \leq 2$. Any Bell inequality bounds correlation that can be observed under the assumptions used to construct it. In the case of the CHSH inequality the assumption is Bell locality (2.11) which is a consequence of assuming remote outcome independence (2.9) and remote context independence (2.10).

The CHSH correlation between the measurement operators $A = \frac{1}{2}(I \pm \sigma_z)$, $A' = \frac{1}{2}(I \pm \sigma_x)$, $B = \frac{1}{2}(I \pm \frac{1}{\sqrt{2}}(\sigma_x + \sigma_z))$ and $B' = \frac{1}{2}(I \pm \frac{1}{\sqrt{2}}(\sigma_x - \sigma_z))$ for the entangled state $|\Psi_-\rangle = \frac{1}{\sqrt{2}}(|01\rangle - |10\rangle)$ is $2\sqrt{2}$, which is the maximum violation of the CHSH inequality predicted by quantum mechanics.

Any Bell test must meet a number of experimental requirements which are referred to as loopholes. Failure to address these loopholes permits local realist explanation of the observed measurement correlation. The three most significant loopholes are; *sampling* loopholes arise when there are inefficiencies in measurement due to loss between source and detectors, particularly, inefficient detection or inefficiencies establishing the coincidence between detections used to calculate correlations; the *locality* loophole arises when there is the possibility of information from measurement on one system influencing measurement on the other; and the *freedom of choice* or *measurement independence* loophole concerns the independence of measurement choice and the internal state of the physical system being measured. Closing the locality loophole is reasonably straight forward by assuring appropriate separation between the detectors but large separations can increase loss making simultaneously closing sampling loopholes difficult.

Heralding efficiency, the probability of detecting one particle in a pair conditioned on detecting the other, is key to closing sampling loopholes without assuming that the loss is fairly sampled. Fair sampling assumes that loss due to measurement inefficiency is *not* biased in a way that enhances measurement correlation in the cases where detection is successful. By assuming the opposite is true, that loss maximally enhances correlation, a new bound for a Bell inequality can be derived[Lar98]. For the CHSH inequality the bound becomes $\frac{4}{\eta} - 2$ where η is the heralding efficiency. A violation of the CHSH inequality by quantum mechanics requires a

heralding efficiency $> 2(\sqrt{2} - 1)$. All early Bell tests using photons were performed under the fair sampling assumption. The unrivaled TES efficiency and lack of dark counts played a key role in recent Bell tests using spontaneous parametric down-conversion (SPDC) as the source of photon pairs [SMSC⁺15][GVW⁺15] that simultaneously close the locality and measurement independence loopholes without assuming fair sampling.

2.1.4 Quantum correlations

Mathematically, entanglement is associated with non-separable quantum states, ie states that cannot be written as a tensor product of subsystems. Non-separable quantum states can be arranged in a hierarchy by correlation strength; Bell non-local states that are capable of a Bell violation; *steerable* states are a super-set that includes the Bell non-local states and can violate a quantum steering inequality. The degree of non-classical correlation increases from non-separable to steerable to Bell non-local states.

Steering is the ability to remotely prepare one subsystem in different ensembles of states by performing different measurements on another subsystem. This concept was introduced by Schrödinger to generalise the EPR paradox for pure bipartite quantum states and is often referred to as EPR steering. Steering was put into a quantum information framework[WJD07] and inequalities developed that limit the level of correlation that can be observed without invoking quantum steering as an explanation, in a similar way that a Bell inequality limits the amount of correlation that can be explained by local realist theories. In quantum information terms, two parties that each receive a subsystem of a bipartite state can violate a steering inequality to certify they share entanglement.

Nonclassical correlation is a considered a fundamental resource powering the advantages quantum information processing provides over its classical counterpart. During the early development of quantum information theory non-classical correlation was thought to be restricted to non-separable quantum states, ie that zero entanglement implied zero non-classical correlation. Later the concept of discord[OZ01] was introduced. Discord is the difference in two classically equivalent expressions for the mutual information between systems. Some separable mixed quantum states have non-zero discord and these states have no classical analogue. Zero discord and zero entanglement became the boundary for classical/non-classical correlation. Recent work[FP12] has compared nonclassicality criteria developed through quantum information theory and those derived from physical constraints on quantum phase space and quasi-probability distributions. It is found that the two approaches yield maximally nonequivalent nonclassicality criteria, implying that non-classical correlations exist in the absence of both entanglement and discord.

We will probe the classical/nonclassical boundary using the number resolving capabilities of TESs and my hardware processor. The entanglement and discord free nonclassical correlation can be found in higher dimensional spaces and a resource for these correlations can be

generated using SPDC. In SPDC a nonlinear crystal is *pumped* by a laser and the crystal spontaneously down-converts a single pump photon into a pair of photons with half the energy. SPDC outputs a two mode squeezed state[KLM01]

$$|\Psi\rangle = \sqrt{1 - |\lambda|^2} \sum_{n=0}^{\infty} \lambda^n |n, n\rangle,$$

where λ is the squeezing parameter and $|\lambda|^2$ is proportional to the pump power. The probability of producing the Fock state $|n, n\rangle$ consisting of n photon pairs is $p(n) = (1 - |\lambda|^2)|\lambda|^{2n}$ and increases with pump power. Quantum information experiments normally use SPDC to approximate a *heralded* source of single photons where detection of a photon in one mode heralds the occupation of the other. This approximation improves with decreasing pump power as the probability of the higher order terms diminishes. These higher order terms are generally avoided as they contribute to noise in a quantum circuit[WGR⁺08]. In our search for nonclassical correlation in the absence of discord and entanglement we will pump the SPDC with as much power as possible as the nonclassical resource depends on terms of all orders.

After phase randomisation to remove any entanglement or discord the resource state is:

$$\rho_{AB} = \sum_n p(n) |n_A\rangle \langle n| \oplus |n_B\rangle \langle n|,$$

where $p(n)$ is the probability of producing n pairs and n_A (n_B) are the number of photons in mode A (B). The projects theorists have devised a game, similar to the GHZ game, where players with access to ρ_{AB} have an advantage over players that have only classical resources at their disposal. Unlike the GHZ state the correlations in ρ_{AB} are not perfect so no foolproof strategy exists but the quantum strategy has a higher probability of winning compared to any classical one. The number resolving capability of TESs is required for an experimental demonstration as the nonclassical correlation exists between the results of each players measurement of the number of photons they have.

2.2 Design goals

My practical introduction to TES was while working on a project that violated a steering inequality[SGdA⁺12]. The High system detection efficiency of TESs enabled an unprecedented heralding efficiency of $\sim 62\%$ and violated the inequality by 48 standard deviations. A record that was only broken in recent Bell tests[SMSC⁺15][GVW⁺15]. To produce a countable signal from the TES output I used a clunky arrangement of equipment we had on hand. Consisting of an analogue constant fraction discriminator (CFD) and nuclear instrumentation module logic both pieces of equipment were designed for nuclear experiments. A long dead-time had to be imposed to ensure the CFD did not trigger on noise during the falling part of the TES pulse which reduced the conditional detection efficiency we could achieve. Despite this, the setup had the advantage of providing near real-time information useful while setting up and tuning the

circuit. The standard technique for analysing TES output involves digitising entire pulses then processing them using software to extract timing and energy information. While the software approach can provide near realtime information for a few channels it is difficult to scale beyond that. The great advantage of processing the entire pulse in software is that it allows arbitrarily complex processing which can provide energy uncertainty close to the limit set by the sensors intrinsic energy resolution.

Experience gained during the steering project informed and motivated my design and the primary goal was to provide realtime detection information in a scalable way while minimising impact on the underlying sensor efficiency. My approach to achieving this goal was to process the signal in hardware rather than software and trade some energy certainty for realtime access to information from larger numbers of sensor channels all operating at the highest detection rates TESs can support. TESs have a wide dynamic range[LGM⁺14] with increasing energy uncertainty as the number of photons detected increases. The processor is designed for quantum information experiments which generally use “single” photon sources and to operate in the region where detections involve less than twenty 820 nm photons. The design process resulted in a library of circuit components that create and transmit a stream of event packets each containing measurements of a detection pulse and a timestamp. The processor as described in this thesis is a particular arrangement of these library components used for evaluation and testing.

A secondary goal was to provide a platform for exploring techniques for extracting information from the TES signal. At one extreme are techniques that use a vector record of the entire pulse and at the other scalar measurements such as pulse height and area that the current processor implementation returns. Software processing of full pulses delivers the best energy resolution which translates into photon number certainty for a particular photon wavelength. Most of the single photon sources we use in the lab have a wavelength no greater than 820 nm and each photon carries relatively high energy. At these shorter wave lengths degraded energy resolution has less effect on number uncertainty due to the higher energy per photon. Preliminary analysis (subsection 3.2.3) of hardware processing indicates the simple pulse area measurement provides sufficient number certainty for the experiments we have planned. The processor can also optionally capture entire pulse records in conjunction with the scalar measurements and this information can be used to improve how the scalar measurements are implemented. The trace information can also be used to develop other hardware implementable measurements returning shorter vectors lying somewhere between the two extremes of scalar and full pulse measurement.

2.3 System overview

The analogue TES signal is digitised by an analogue to digital converter (ADC) which outputs a sequence of 14 bit integers called samples. The ADC sequence is labeled raw_{in} and each sample

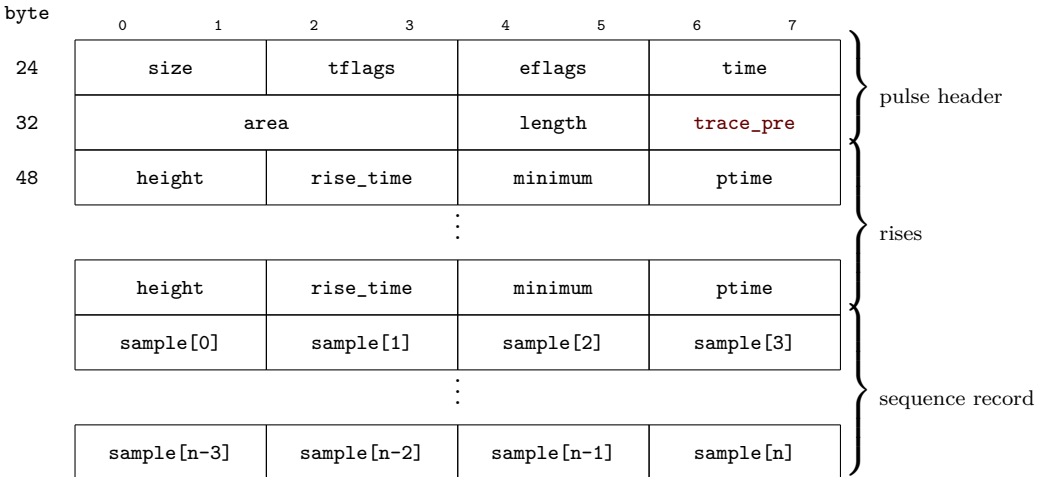
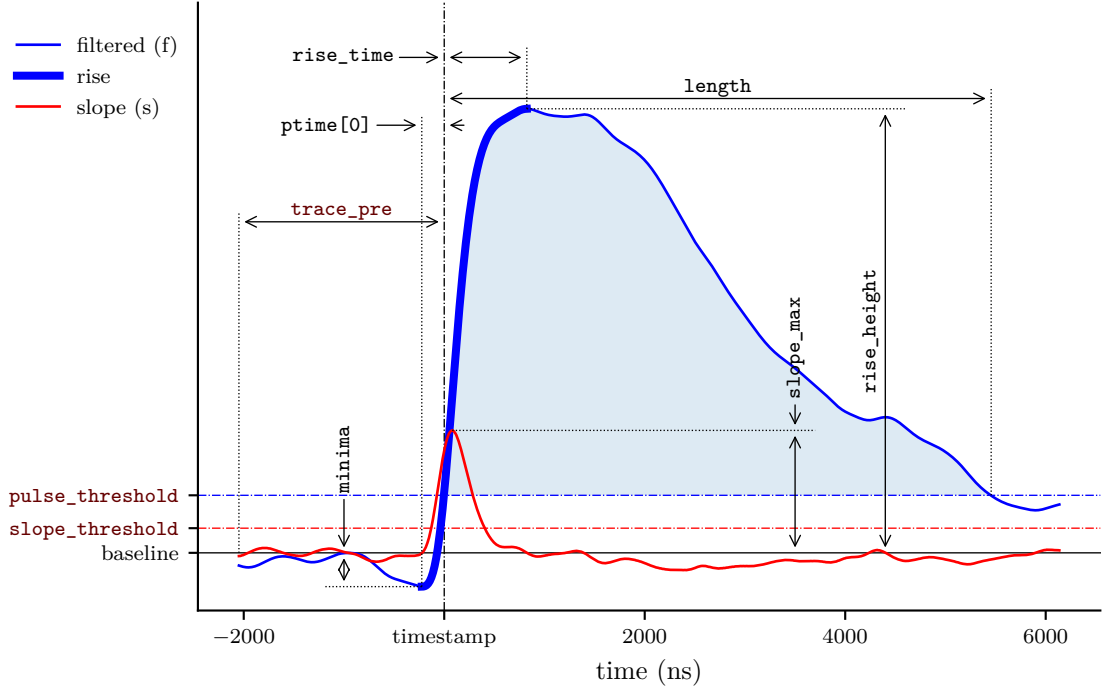


Figure 2.1: Measurement is based on detecting rises in the filtered TES signal (**f**). Zero crossings of the slope (**s**) identify the local minimum and maximum of **f**. Rises are sub-sequences of **f** extending from a minimum to the following maximum and are considered valid when the height exceeds **pulse_threshold** and **s** has crossed **slope_threshold** during the rise. A pulse is a sub-sequence of **f** from the start of a valid rise to the next falling crossing of **pulse_threshold** by **f**. Measurements are performed on each pulse and returned in an event packet along with a timestamp and optionally a sequence record. The shaded region is returned as the **area** measurement. The **height** register controls what appears in the **height** field, for example it can record **slope_max** instead of **rise_height**. More details of the measurement process can be found in ?? and descriptions of the registers controlling measurement in ??

estimates the average voltage at the ADC input over a ~ 4 ns time window and 250 million samples are produced per second. The processor operates on **raw_{in}** and derives other sequences

from it in order to extract detections and energy measurements. See ?? for details.

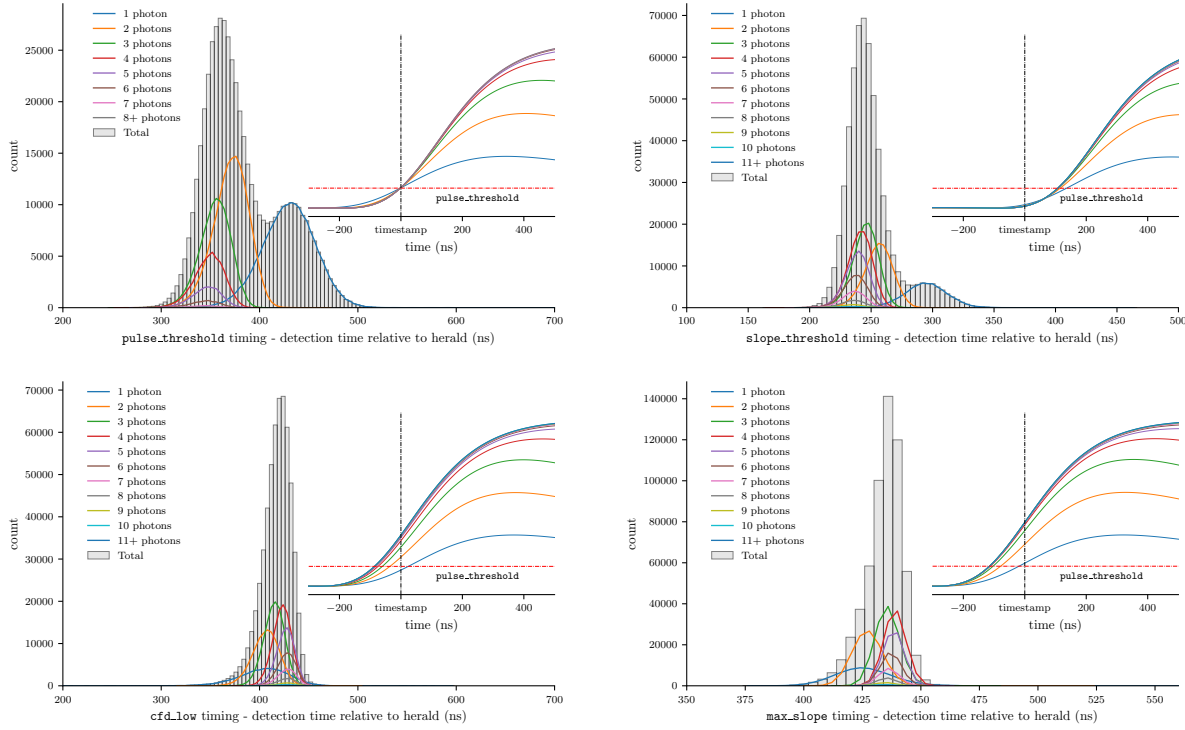


Figure 2.2: The **timing** register controls the point in a rise that is timestamped. The individual panels show histograms of the difference in timestamps from two processor channels. One channel processes the output from a TES while the other channel processes the same electrical pulse that drives the laser diode and heralds possible detections. Grey histograms show the distributions of the relative times between detections and the herald regardless of assigned photon number while the coloured histograms show the distribution of times for detections assigned the respective photon number. The bin width of the histograms is 4 ns which is temporal resolution of the processor. The insets show the alignment of traces under the different **timing** settings, each coloured curve in the inset is the average over all captured traces assigned the respective photon number. The photon number classification process described in subsection 3.2.3. Note that these timing diagrams are not necessarily taken using the same optical inputs or the same TES. Conditions differ between diagrams and the datasets in subsection 3.2.1 and are only a guide to the different forms the number dependant timing jitter takes with different **timing** register settings.

The two most important derived sequences are the outputs of a reconfigurable two stage finite impulse response (FIR) filter (see ??). The first stage is configured as a low pass filter to remove high frequency noise and produces the filtered sequence—labeled **f**—which is the sequence that is measured. The second stage is configured as a differentiator and produces the slope sequence—labeled **s**—which is used to identify *rises* in **f** and establish which rises constitute a *detection*.

Zero crossings of **s** are used to identify rises. Rises are sub-sequences of **f** that extend from a

local minimum, identified by a rising zero crossing of \mathbf{s} , to the next local maximum at the next falling zero crossing of \mathbf{s} . A rise is *valid* and considered a detection when its maximum is above `pulse_threshold` and \mathbf{s} has crossed `slope_threshold` during the rise. A *pulse* starts at the beginning of a valid rise and extends to the next falling crossing of `pulse_threshold` by \mathbf{f} (see Figure 2.1). For each pulse the processor returns an event packet containing measurements of the pulse, a timestamp and optionally a sequence record. The sequence record, called a trace, starts `trace_pre` samples before the timestamp and records every `trace_stride` + 1 sample from the start until `trace_length` samples are recorded. The point at which the timestamp is generated is controlled by the `timing` register, see Figure 2.2. Section ?? describes of the contents of the different types of event packets, ?? provides details of the measurement processes and ?? describes the registers that control the processor.

2.3.1 The multi-channel analyser (MCA)

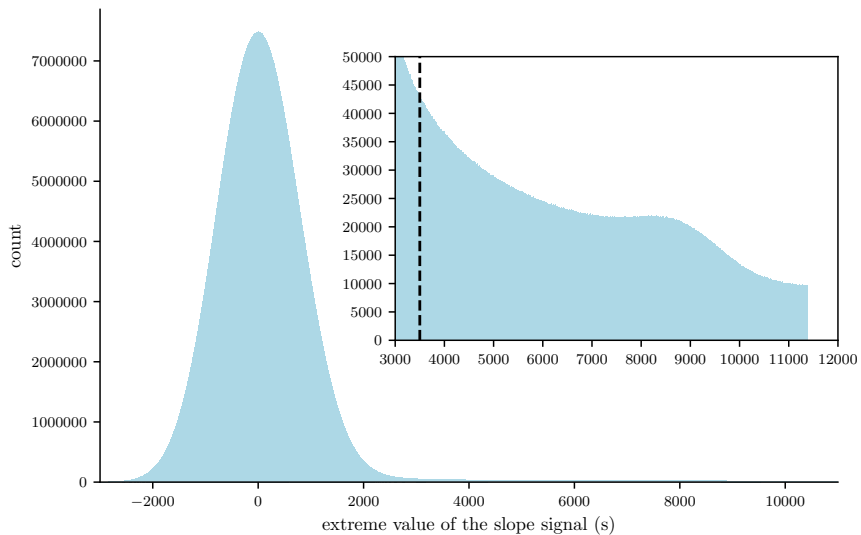


Figure 2.3: Distribution of the filtered TES sequence, \mathbf{f} , captured by the multi-channel analyser (MCA). The MCA is capable of accumulating samples at the 250 million samples a second rate produced by the ADCs, so the histogram counts the frequency of every integer in the sequence \mathbf{f} . The main body of the distribution represents the noise produced by the TES and associated electronics, the long tail on the right is due to the optical signal. The inset shows a zoomed view on the optical signal which continues past the abrupt termination at the last MCA bin. The vertical dashed line indicates the `pulse_threshold` setting.

The processor includes a MCA, which is a rather anachronistic term for a device that gathers the distribution of a measurement as a histogram. My MCA design is capable of counting every sample of a sequence while continuously transmitting the distribution of the sequence to the host computer (see Figure 2.3). It is of particular use in determining threshold register settings and descriptions of the registers controlling the MCA can be found in ??.

Measurements and settings are relative to a *baseline* assigned the value 0. A design assumption is that the baseline should be at the *mode* of the distribution of \mathbf{f} (Figure 2.3). AC coupling to the TES output preamplifier (Figure 1.2) sets the 0 volt value at the *mean* of the \mathbf{f} distribution. The position of the mean relative to the mode is dependant on the power of the optical input. This is due to the unipolar nature of the pulses which make the \mathbf{f} distribution asymmetric with a long tail on one side. A simplified version of the central MCA is incorporated into each channel to track the mode of the \mathbf{f} distribution and adjust the baseline accordingly (see ??). This technique was not implemented to correct the baseline on short time scales but to correct for changes in output power seen when collecting experimental data. For example, when performing tomographic set of measurements the power to the sensor can vary widely with measurement setting. I discuss baseline correction further in section 4.1.

Chapter 3

Preliminary testing and analysis

3.1 Test apparatus

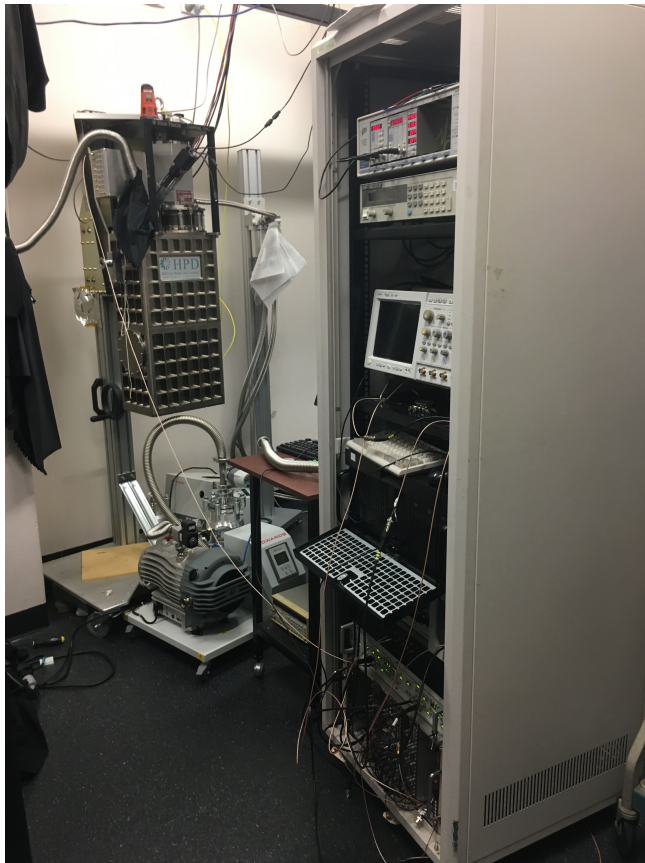


Figure 3.1: The cryostat and control electronics rack: The ADR stage and TESs are housed in the silver box labeled HPD. The rack of control electronics is in the foreground and the FPGA development board and ADC card used to implement the processor are installed in a case low in the rack. The silver pipe exiting the top of the HPD box carries fibres connected to TESs to the light tight fibre junction box out of frame on the left. In the junction box fibres from the TESs can be sliced to fibres connected to experiments.

We use an ADR to get our TESs down to operating temperature. An ADR is a final

low temperature cooling *stage* usually housed in a continuous closed cycle refrigerator. Our continuous cycle refrigerator is a pulse tube refrigerator (PTR) [dW00] with a cold plate at $\sim 3\text{ K}$ and the ADR stage cools from 3 K down to the TES operating temperature. ADRs utilise the magnetocaloric effect by controlling the entropy of the magnetic moments of a paramagnetic salt housed in *pill*. Energy in the magnetic degrees of freedom of the pill is dependant on the angle of the magnetic moments relative to the direction of an external magnetic field and that fields strength. The minimum energy configuration occurs when all the magnetic moments are aligned with the field. The pill is suspended inside the PTR below a superconducting magnet which provides the field and the pill can be either thermally isolated or connected to the 3 K plate by opening or closing a mechanical *heatswitch*.

In order to cool the TESs, which are attached to the pill, down to operating temperature the ADR must first be magnetically *cycled*. During the magnetisation phase of the cycle the field is slowly increased over a period of ~ 15 minutes with the heatswitch closed¹. As the field increases the entropy of the pill decreases as the moments align with the field. Energy stored in the misalignment of the moments moves into vibrational degrees of freedom of the salt molecules increasing the pills temperature. Entropy moves from magnetic degrees of freedom to thermal degrees of freedom. By the time the magnet reaches full field the pill temperature is a few degrees above the 3 K plate. The pill is then *soaked* at full field for at least an hour, during the soak phase heat flows from the pill through the heatswitch to the cold plate and the pill cools towards 3 K . The heatswitch is then opened isolating the pill and the field is decreased over a period of about 20 minutes in the adiabatic demagnetisation phase of the cycle. As the field decreases the magnetic moments are knocked out of alignment by thermal motion absorbing the thermal energy and cooling the pill. Entropy moves from the thermal degrees of freedom to the magnetic degrees of freedom. The temperature of the pill and attached TES can be controlled by adjusting the current in the magnet which alters the field strength. When the pill temperature reaches the desired operating temperature control of the power supply providing the magnet current is handed over to a proportional-integral-differential (PID) controller to regulate the temperature.

While the PTR has a cooling *power* capable of maintaining a temperature indefinitely under a thermal load of less power, the ADR stage has a cooling *energy* and can only maintain a temperature under any load for a finite *hold* time. With a roughly 90 minute cycle our system has approximately 8 hours of hold time at 100 mK . Although I have fully automated the cryostat by adding a motor to operate the heatswitch and developing software so the cryostat

¹ If the current in the superconducting magnet is changed too rapidly the protection circuit will activate due to the back EMF. When the voltage across the magnet leads exceeds $\sim 0.7\text{ V}$ the circuit shorts the magnet. This protects personnel and external equipment if there a loss of cooling power or another event that causes the magnet to stop superconducting while significant field current is flowing. Without the circuit the energy stored in the magnetic field would exit the cryostat via the magnet power leads in a high current and voltage pulse in a process called a magnet *quench*.

can be monitored and controlled remotely from the same script controlling an experiment, the cryostat adds an extra layer of complication to experiments involving TESs.

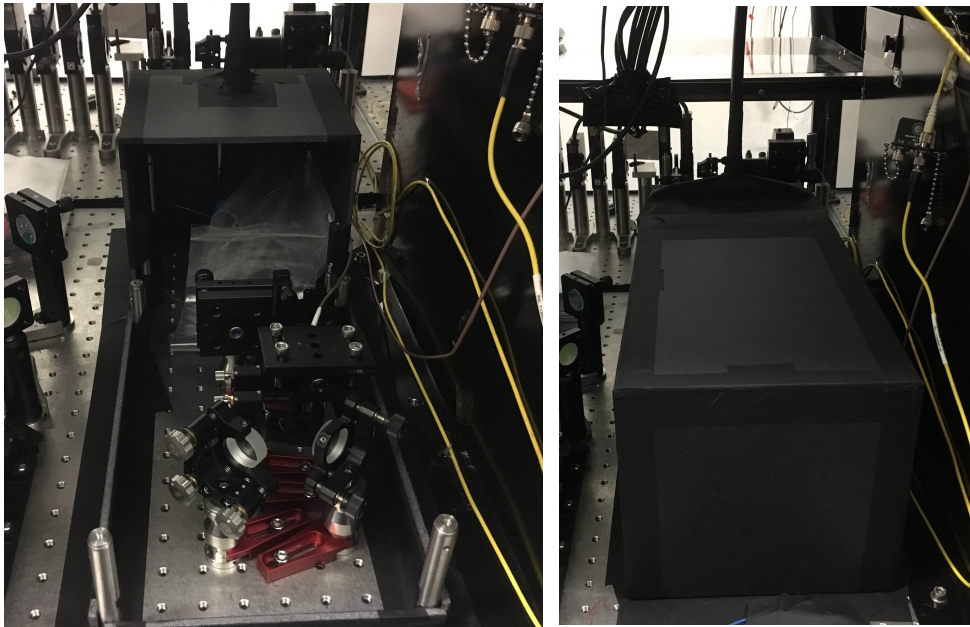


Figure 3.2: Test source: The source of weak optical pulses used for testing is a nominally 820 nm laser diode driven by a 50 ns 2.6 V electrical pulse at 10 kHz from a pulse generator. The diode and associated optics are housed in a light tight box and fibres run from the box to TES in a light tight conduit. Unused fibres connected to TESs are in the plastic bags seen at the back of the box. The diode output (middle right) passes through a 2 nm wide spectral filter centered at 820 nm (not shown). After the filter the beam is steered by two mirrors (front) through two linear polarisers, which provide variable attenuation to adjust the average photon number in a pulse, to the fibre coupler leading to the TES (middle left just in front of the plastic bags).

The optical input used to analyse the processors performance is provided by an \sim 820 nm laser diode driven by a 50 ns wide 2.6 volt electrical pulse at 10 kHz. The laser output is filtered by a 2 nm wide spectral filter centered at 820 nm. The diode and associated fibre coupling optics are housed in a light tight box (Figure 3.2) and fibres to the TES run through a light tight conduit. Fine control of the pulse intensity is achieved with a pair of linear polarisers.

3.2 Preliminary performance analysis

3.2.1 Data acquisition

The TES system output from the $\times 100$ preamp (Figure 1.2) is AC coupled to Lecroy model 1855A amplifier for further amplification before being passed to the ADCs attached to the FPGA. Data was captured during same hold cycle of the ADR with four levels of optical attenuation² (see Table 3.1). A second processor channel measures the electrical pulse driving

² The names indicate the dominant photon peak on the live MCA display as I adjusted the attenuation.

Dataset	Events captured	Model distributions	Acquisition time (s)
peak4	17834243	15	1800
peak3	17744605	14	1800
peak2	16960239	11	1800
peak1	14894211	8	1800

Table 3.1: Data capture details. The captures are of `pulse` event packets. Shorter (1 minute) captures of `single_trace`, event packets which include a record of `f`, were also taken to create figures containing traces. The model distributions column indicates the maximum photon number assignment in the measurement model for that dataset.

the laser to be used as a herald of possible detections.

The processors central MCA can capture a wider set of measurements than can be returned in event packets. In particular it is not constrained to measurements of *valid* rises or pulses as determined by the `pulse_threshold` and `slope_threshold` registers, see Figure 2.1. The extrema sequences are the extreme value of a sequence since its previous zero crossing. The `f_extrema` and `s_extrema` sequences are used to find appropriate settings for the `pulse_threshold` and `slope_threshold` registers. See Figure 3.3 and Figure 3.4. The thresholds were set so that some noise is captured in the datasets.

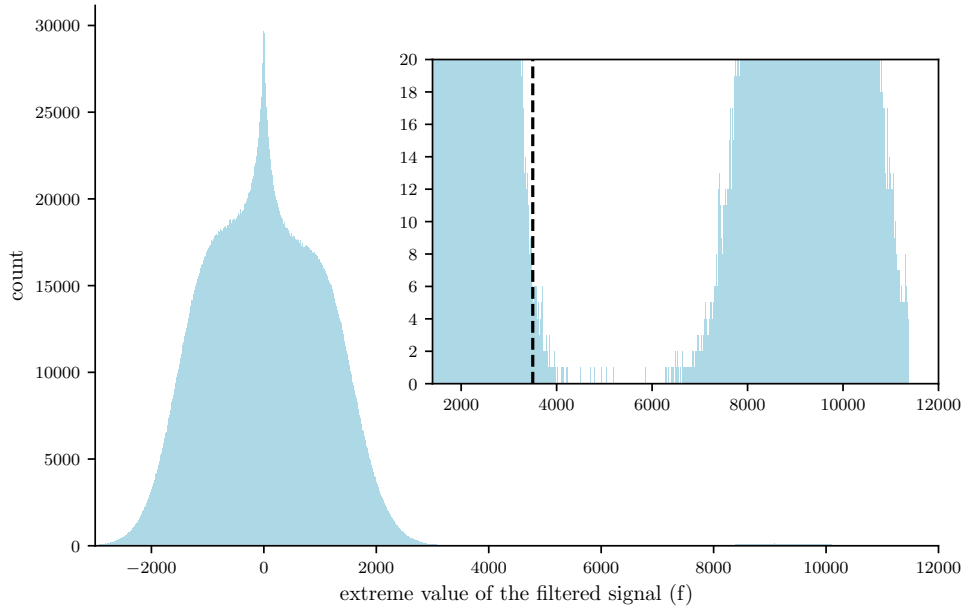


Figure 3.3: Distribution of `f_extrema` signal. `f` is the extreme value of `f` since its previous zero crossing but the figure only shows the distribution of the maximum. The inset shows a zoomed in view with the distribution of the noise on the left and the single photon distribution on the right. The vertical line indicates the `pulse_threshold` is set into the tail of the noise distribution.

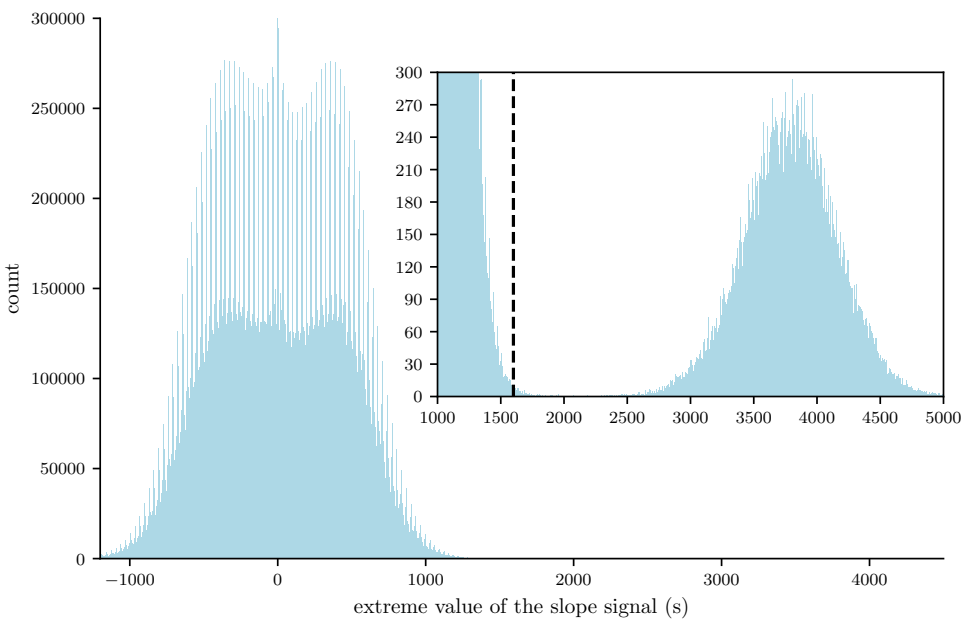


Figure 3.4: Distribution of `s_extrema` signal. `s` is the extreme value of `s` since its previous zero crossing but the figure only shows the distribution of the maximum. The inset shows a zoomed in view with noise on the left. The peak on the right is distribution of the maximum value of `s` during detection of a single photon. The vertical line shows `slope_threshold` is set just into the noise distribution. I believe the fine structure in the distribution is because the `s` sequence is rounded to a 16.8 bit (16 bit wide with 8 fractional bits) value at the output of the differentiator. Many of the fractional bits are not significant and there is a periodic variation in the probability that the filter stages generate values over the 16 bit range. The distribution becomes smooth when MCA `bin_n` register is used to increase the histogram bin width.

3.2.2 Dark noise

In its current location in the lab our TES are often plagued by electromagnetic interference. I've done what I can to trouble shoot the problem and improve earthing without success. To collect the data I limit the signal bandwidth to 1 MHz using the analogue input filters in the Lecroy amplifier's input stage, this removes most of the interference. Unfortunately the restricted input bandwidth also limits the utility of the `s` sequence in discriminating between noise and true photon detections.

Figure 3.5 displays traces captured over 30 minutes with the laser diode off and includes events with higher energy than seen even with the laser is on. I speculate that these are cosmic ray related as generally they rise and cool a slower rate than a photon absorption which may indicate energy absorbed near the sensor heating it more slowly. Most of the events detected with the laser off are a combination of TES noise and photons from the high energy tail of the blackbody spectrum. A few photons from the lab still manage to couple into the fibre leading to the sensor, the rate is very low, ~ 1 event every 10 minutes³.

³ We have a more sensitive TES that has not been fully analysed, it has higher intrinsic gain and gives better

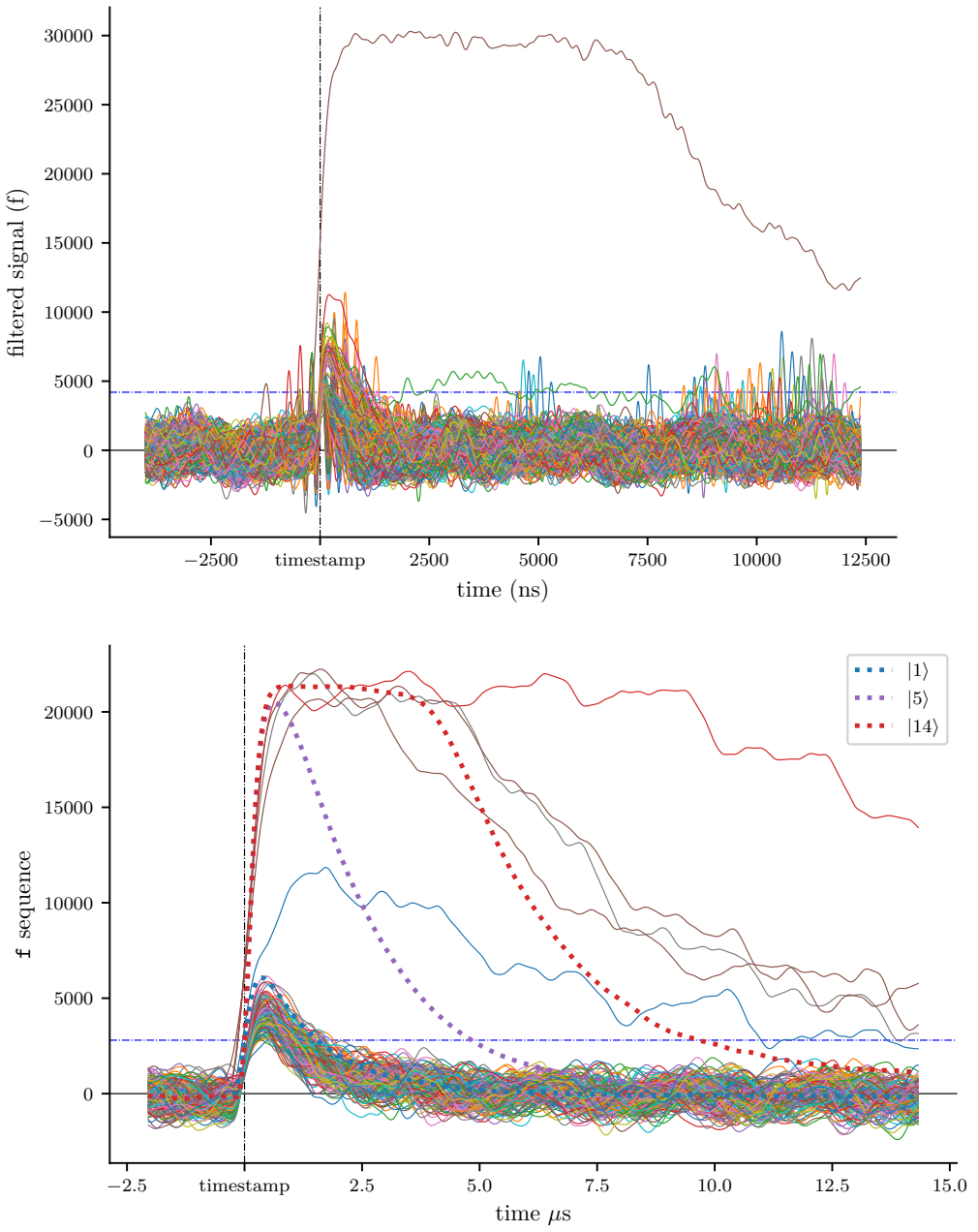


Figure 3.5: Dark traces captured over 30 minutes with 30 MHz (top) and 1 megahertz (bottom) bandwidth at the input of the Lecroy amplifier. The dash-dot blue line indicates the `pulse_threshold` setting. The thick dotted lines indicate the average pulse shape found by first assigning a photon number to traces using techniques described in subsection 3.2.3 then averaging over all traces assigned the same photon number. The majority of the 141 dark events captured during the 30 minutes are due to a combination of blackbody photons and intrinsic TES noise.

3.2.3 Statistical modeling

This analysis focuses on the pulse `area` measurement as it has the highest dynamic range. The techniques can also be applied to the other measurements such as rise height, maximum slope

discrimination between the blackbody and 820 nm photons.

etc.

If a magic box that emitted a known photon number (Fock) state at the press of a button existed, I could use it to characterise the the performance of the TES and processor. Repeatably pressing the button that emits a single photon would enable the distribution of area measurements for single photon detections to be determined. Pressing the two photon button allows the two photon measurement distribution to be estimated etc. The parameters of each distribution are dependent on the energy of the measured Fock state, the sensors energy resolution at that energy, the intrinsic TES noise and noise added by electronics and the **area** measurement process. In the absence of magic the best I can do is input an unknown Fock state superposition.

The Expectation Maximisation (EM) [DLR77] algorithm computes a Maximum Likelihood (ML) estimate in the presence of hidden data. I use it to fit a a mixture model made up of multiple component distributions to the measurement data. In this case the hidden data is the weight of each component in the mixture which originates from the unknown Fock state superposition generated by the pulsed laser diode (Figure 3.2).

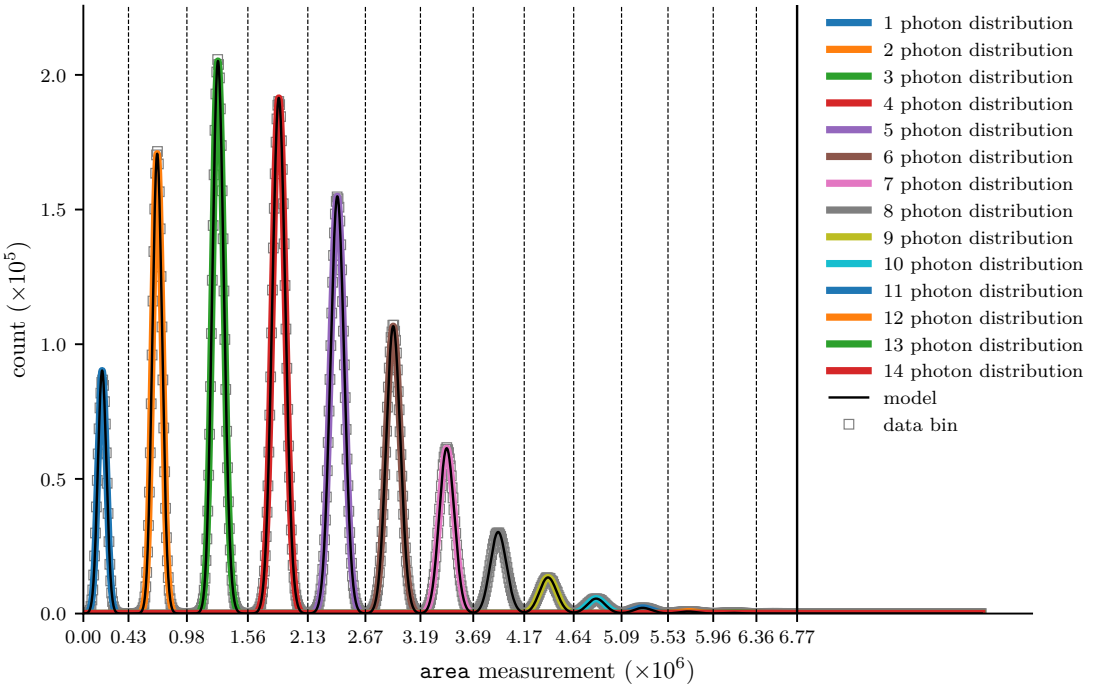


Figure 3.6: The **area** measurement model created from the peak3 dataset. The distribution of measurement values is modeled as a mixture of gamma distributions which are fitted using the expectation maximisation algorithm, see text for details. The algorithm finds the maximum likelihood estimates of each distribution's parameters and its weight in the mixture by systematically adjusting thresholds (dashed vertical lines) that partition the population of measurement values into sub-populations belonging to individual distributions. Only measurement values less than solid vertical line are fit to distributions but the total number of values is used in the calculation of the weights.

I implement the simplest form of the algorithm:

- The maximisation step takes a set of thresholds that partition the measurement values into sub-populations. Each sub-population is assumed to be sampled from one distribution in the mixture. ML estimates of the parameters for each distribution are then calculated from each sub-population and the proportion of the total measurement values each sub-population represents serves as an estimate of the hidden data.
- The expectation step uses the distribution parameters and hidden data estimated at the previous maximisation step to update the thresholds. New thresholds are set by finding the intersection of the probability density functions (PDFs) for each neighbouring distribution.

Maximisation and expectation are iterated over until the likelihood of the mixture model converges. When the individual distributions in the data are well defined and reasonable initial thresholds are supplied this simplified EM procedure performs well. A set of initial thresholds used to seed the EM algorithm is found by first constructing a histogram from the measurement value population, convolving it with a smoothing filter and then finding the peaks of the smoothed histogram. Initial thresholds are set at the midpoint between the discovered peaks with two additional thresholds added to bound the range of measurement values used by the algorithm. An initial threshold at 0 set the lowest value used and one symmetrically placed after the last discovered peak sets the highest value used. These bounding thresholds remain fixed during the expectation maximisation process.

To compare models I use the Akaike information criterion (AIC) [Aka98],

$$AIC = 2k - 2 \ln(\hat{L}),$$

where k is the number of degrees of freedom of the model and \hat{L} is the maximum of the likelihood function. The AIC is an asymptotically valid estimate of the information lost by a model of some unknown distribution. When two models are compared the one with the lower AIC is preferred. The relative likelihood is,

$$\exp\left(\frac{AIC_1 - AIC_2}{2}\right),$$

where AIC_1 is the lower AIC of the two models. The relative likelihood estimates the probability that the model with AIC_2 minimises the information loss rather than the model with AIC_1 .

Comparing measurement models composed of Gaussian, skewed Gaussian and gamma distributions the relative likelihood establishes that a mixture of gamma distributions is the most likely of the three model types to minimise information loss. The **area** measurement model constructed from the peak3 dataset is shown in Figure 3.6.

Counting thresholds are found using a measurement model consisting of M distributions by normalising them and calculating the intersection of the neighbouring PDFs. These $M - 1$

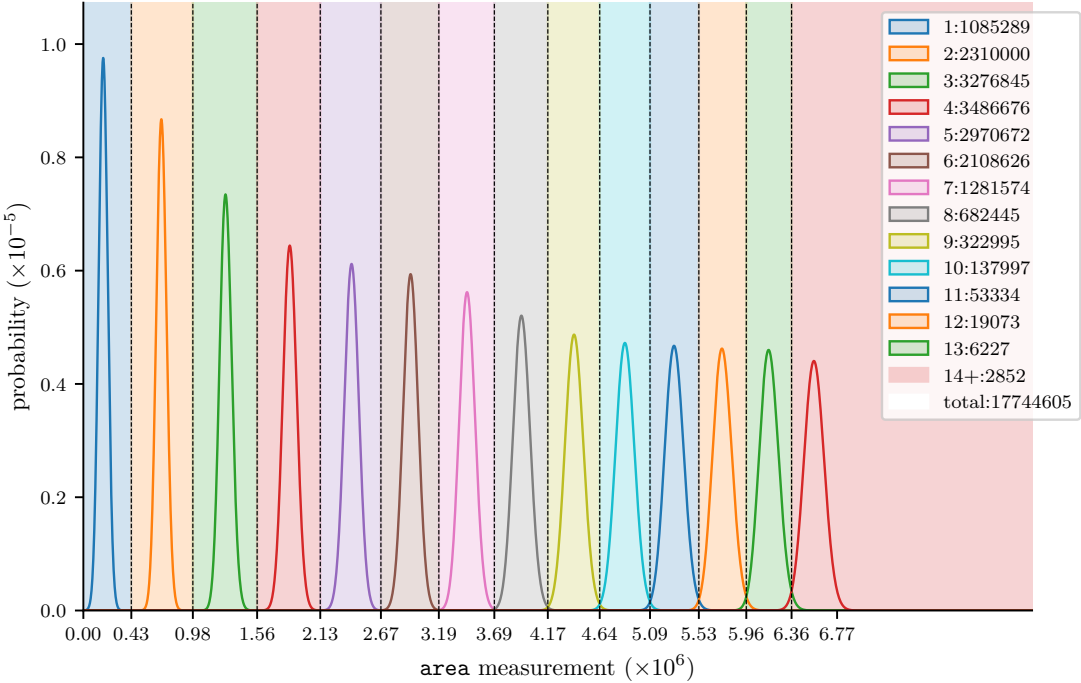


Figure 3.7: *Counting* thresholds are found by normalising each of the M distributions in the measurement model and calculating the intersection of the neighbouring PDFs. Photon number M_+ is assigned to all measurements greater than the $(M - 1)^{th}$ threshold indicating detection of at least M photons, see text for details. The figure shows the model constructed from the peak3 dataset and the numbers in the legend count the measurements assigned to each photon number.

thresholds are labeled t_n where $n \in [1, M - 1]$ and are used to assign photon number n to measurement value a . When $a \leq t_{M-1}$ it is assigned photon number n where $t_{n-1} < a \leq t_n$ and $t_0 \equiv 0$. When $a > t_{M-1}$ it is assigned the photon M_+ indicating a detection of *at least* M photons, see Figure 3.7.

Probabilities for assigning the photon numbers to a measurement value can be found from the overlap of the distributions in a measurement model, see Figure 3.8. By using the values of the cumulative density functions (CDFs) of the distributions at the modeled counting thresholds an operator that takes an input Fock state superposition to a superposition of photon number assignments (measurement outcomes) can be created. Let p_n^f be the probability of assigning photon number n to a measurement of Fock state f , then

$$p_n^f = \begin{cases} cdf_f(t_n) - cdf_n(t_{n-1}) & f \leq M, n < M \\ 1 - cdf_f(t_{M-1}) & f < M, n = M \end{cases}$$

$$p_x^f = \begin{cases} 1 & f > M, x = M \\ 0 & f > M, x \neq M \end{cases} \quad (3.1)$$

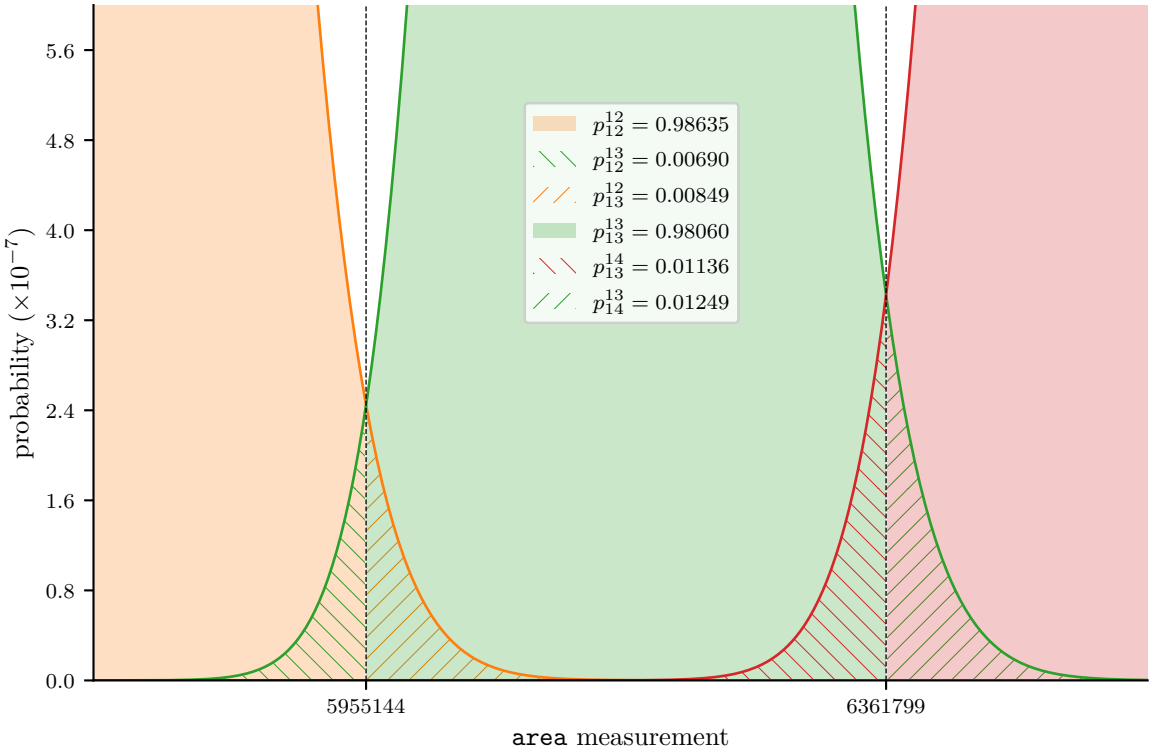


Figure 3.8: By using the values of CDFs of the distributions at the thresholds a the probabilities of assigning the wrong photon number to a measurement can be estimated. These probabilities can be used to estimate the the superposition of assigned photon numbers that arises from measuring a given Fock state superposition. The probability p_n^f is the probability of assigning photon number n to a measurement of Fock state f .

and we have

$$\sum_{i=1}^M p_i^f = 1 \quad (3.2)$$

These number assignment probabilities can be used to construct an operator similar⁴ to a positive-operator valued measure (POVM), an operator used to describe generalised quantum measurement, which maps the state measured to measurement outcomes, see Figure 3.8.

As an operational test I reconstructed the laser's output state from the number resolved counts and the heralding information provided by the laser drive pulse. Vacuum counts are found by counting the number of heralds that are not correlated with a detection, see Figure 3.9 and Table 3.2. The laser output (Figure 3.2) is modeled as a two parameter Gaussian state

$$\rho_{\alpha, \bar{n}} = D(\alpha) \rho_{\bar{n}} D(\alpha)^\dagger, \quad (3.3)$$

where $D(\alpha)$ is the displacement operator and $\rho_{\bar{n}} = (1 - e^{-\bar{n}}) \sum_n e^{-\bar{n}n} |n\rangle \langle n|$ is a thermal state with average photon number \bar{n} . When $\bar{n} = 0$ $\rho_{\alpha, \bar{n}}$ is a coherent state. To create the the laser

⁴There are no probabilities related to the vacuum outcome which may disqualify it as a true POVM

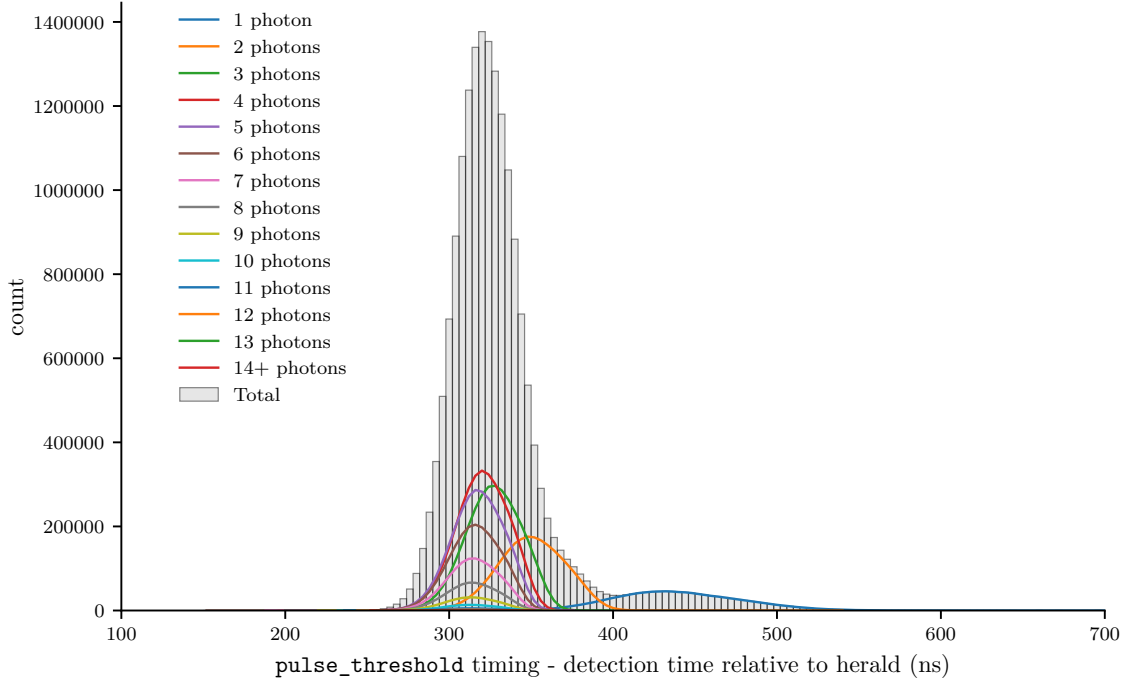


Figure 3.9: The datasets are captured with the `timing` register set to `pulse_threshold`. The histogram records the relative delay between a detection and a heralding signal derived from the electrical pulse that energises the laser diode. The probability of a vacuum detection is estimated as the number of heralding events not coincident with a detection divided by the number of heralding events in the dataset. A coincidence occurs when there is a detection between 100 ns and 700 ns after the herald.

	Correlated detections		Uncorrelated events		
	total	1-photon	heralds	1-photon	multi-photon
peak4	17833759	775469	166387	473	11
peak3	17744142	1085289	256007	458	5
peak2	16959820	2967401	1040327	416	3
peak1	14893808	5448324	3106340	399	4

Table 3.2: Temporal correlation between the heralding signal derived from the pulse driving the laser and TES detections. The photon number dependent jitter is shown in Figure 3.9. When the delay between the herald and detection is between 100 ns and 700 ns the herald and the detection are considered correlated and coincident. Uncorrelated heralds are considered vacuum detections.

output state estimates in Figure 3.10, I use the measurement model created from the peak3 datasets to analyse *all* four datasets to test how a single calibration performs with different optical inputs to the TES. I use a parametrised model of $\rho_{\alpha,\bar{n}}$ created with QuTiP[JNN13] to calculate the Fock state superposition probabilities, then apply the number assignment error

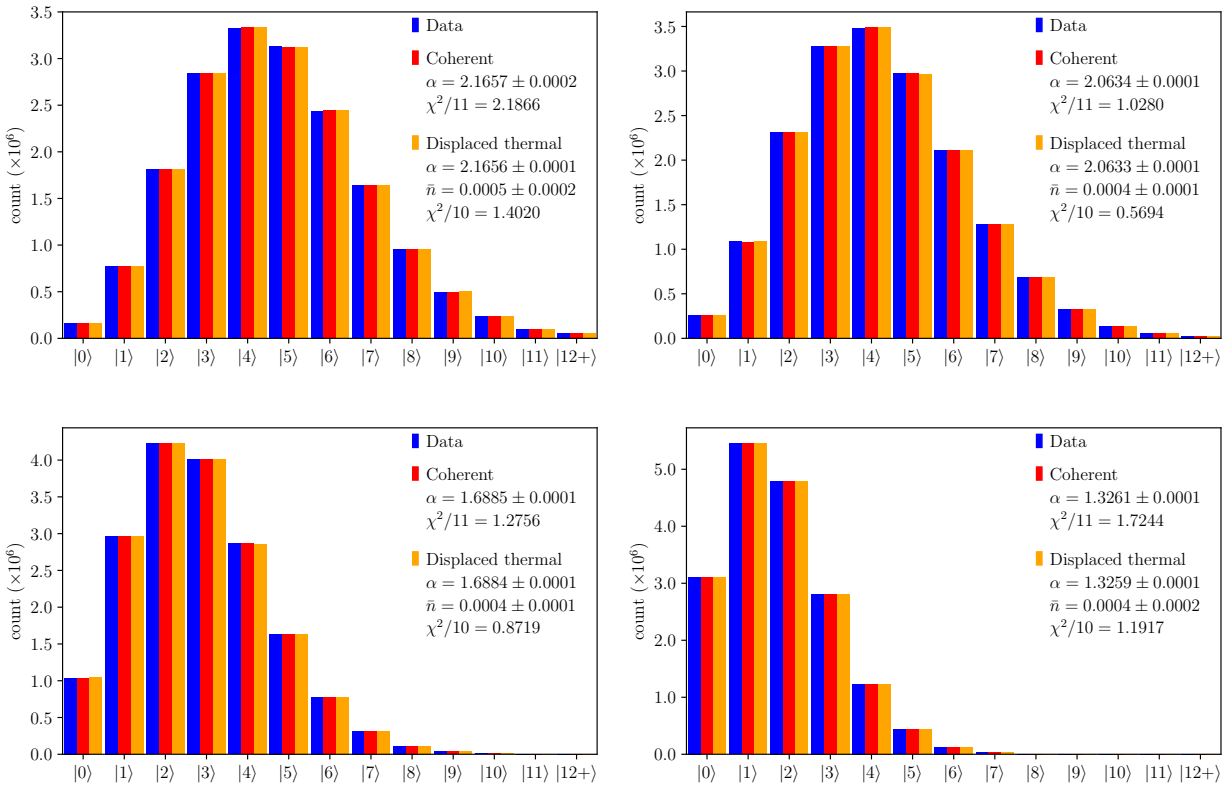


Figure 3.10: Least squares fitting of the datasets to model the optical input states. The datasets are peak4, peak3, peak2 and peak1 from left to right and top to bottom. Number assignment probabilities (Equation 3.1) and counting thresholds (Figure 3.7) from the measurement model created from the peak3 dataset are used to analyse *all* datasets. The number assignment probabilities are applied to the Fock state superposition produced by a parametrised model of a displaced thermal state ($\rho_{\alpha,\bar{n}} = D(\alpha)\rho_{\bar{n}}D(\alpha)^\dagger$) to estimate the measurement outcome probabilities. Measurement outcomes are contracted from $1-14_+$ to $1-12_+$ to minimise truncation effects due to the finite measurement model. The α and \bar{n} parameters are estimated by non-linear least squares minimisation of the residuals between the modeled and observed measurement outcomes. The vacuum detection probability is estimated from the number of laser drive pulses not coincident with a detection, see Figure 3.9 and Table 3.2. Standard errors are calculated from an estimate of the covariance matrix created by the least squares minimisation. The coherent state model has a fixed $\bar{n} = 0$.

probabilities (POVM) in Equation 3.1 and contract the result from number outcomes $1-14_+$ to $1-12_+$ in order minimise truncation effects. To estimate the parameters of $\rho_{\alpha,\bar{n}}$ I perform a non-linear least squares minimisation⁵ of the residuals between modeled and observed measurement outcomes. Figure 3.11 assumes the laser outputs coherent states and examines the stability of the state estimate over time. Each dataset is broken into subsets containing 100000 laser drive pulses and the α parameter is estimated as described above for each subset. Table 3.3 and

⁵ Using the LMfit package which wraps the SciPy minimiser calling the MINPACK implementation of the Levenberg–Marquardt algorithm[Lev44]

Table 3.4 contain estimates of mean and standard error of the laser output state parameters from the subset populations plotted against time in Figure 3.11.

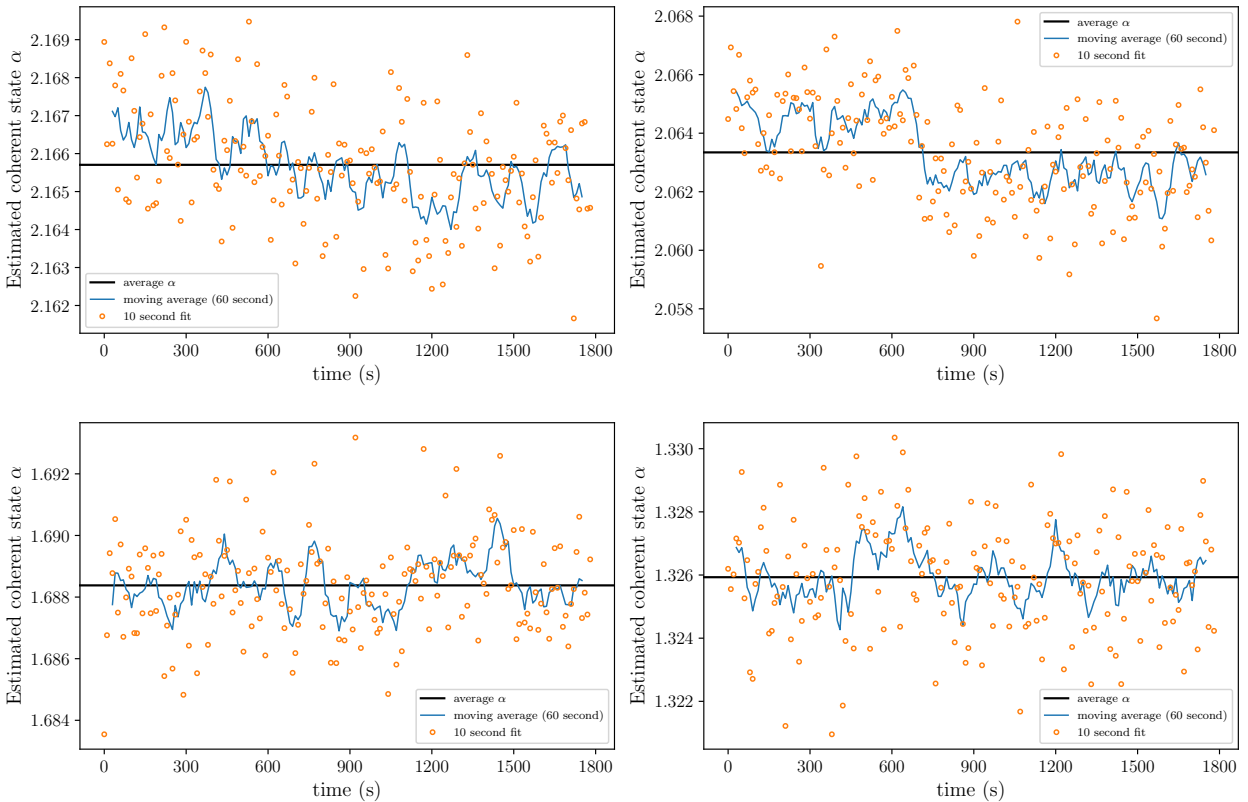


Figure 3.11: The stability of the coherent state estimate. Each data set is broken into subsets containing 100000 laser drive pulses, representing a 10 second capture time, and the subset is used to estimate α as described in the text. The blue line is a moving average over 6 of the 10 second estimates.

	100000 heralding events (10s)		running average (60s)	
	Coherent state α	$\chi^2/11$	Coherent state α	$\chi^2/11$
peak4	2.166 ± 0.002	1.0 ± 0.4	2.1657 ± 0.0008	1.0 ± 0.1
peak3	2.063 ± 0.002	1.0 ± 0.4	2.063 ± 0.001	1.0 ± 0.2
peak2	1.688 ± 0.002	1.0 ± 0.5	1.6884 ± 0.0007	1.0 ± 0.2
peak1	1.326 ± 0.002	1.0 ± 0.6	1.3257 ± 0.0007	1.0 ± 0.2

Table 3.3: Coherent state estimates based on the statistics of subsets containing 100000 drive pulses, values are recorded as $(\text{mean}) \pm (\text{standard deviation})$ from the population of estimates plotted against time in Figure 3.11.

100000 heralding events (10s)			
	α	\bar{n}	$\chi^2/12$
peak4	2.165 ± 0.002	0.001 ± 0.001	1.0 ± 0.4
peak3	2.063 ± 0.002	0.001 ± 0.001	1.0 ± 0.5
peak2	1.688 ± 0.002	0.001 ± 0.001	1.1 ± 0.5
peak1	1.326 ± 0.002	0.001 ± 0.001	1.1 ± 0.7

Table 3.4: Thermal state estimates from the statistics of subsets of each dataset containing 100000 laser drive pulses. Values are recorded as (mean) \pm (standard deviation) of the subset population.

Chapter 4

Discussion and conclusions

4.1 Discussion

The accuracy of the scalar measurements the processor currently makes hinge on the accuracy of the baseline estimate. While capturing the peak4 dataset, the baseline shifted by approximately 400 from its value when the laser was off. The estimate of $\alpha = 2.166$ for the weak coherent pulses captured in peak4 implies an average rate 46920 photons per second. Though the dynamic correction described in subsection 2.3.1 was active (`baseline.dynamic=True`) the correction mechanism operates on comparatively long time scales. Baseline error effects the `area` measurement in an outcome dependent way. It adds area noise proportional to the length of the TES detection pulse which is correlated with the measured Fock state. Two major factors influence the quality of the laser output state estimations in Figure 3.10, Figure 3.11, Table 3.3 and Table 3.4, one is baseline error the other is errors in discriminating photon detections from noise.

Baseline correction through monitoring the mode of the `f` sequence is novel but was only intended as a first approximation to be used in the initial peak finding pipeline. A second order estimation can be made for each detection by adding some extra delay and pipelining enabling averaging over the `f` sequence over a fixed time range before the timing point of each pulse. The current prototype would be used to establish where and for how long the average should be acquired and what improvement in measurement uncertainty could be achieved.

Figure 3.11 displays the stability of the estimate of the laser output state over time. Each dataset in the figure was captured over a 30 minute period in the following order peak4, peak3, peak2 then peak1, time flows left to right top to bottom. Given that there is no temperature stabilisation of the laser diode, the drift in intensity seen in Figure 3.11 is consistent with a drift in the laser's wavelength as it thermalises. Wavelength drift is converted into drift in the average photon number per pulse by the 2 nm wide filter. In this scenario, the abrupt drop in α in the middle of the peak3 dataset can be attributed to a mode hop. An alternative explanation is that the drift in the estimated pulse intensity is due to drift in the baseline estimate. Though I favour the former explanation, the true picture most likely involves a combination of the two.

Further investigation is required and the processor is capable of capturing `pulse` packets, as was done to collect the datasets, while simultaneously capturing distributions streamed from the MCA. These two datastreams can be correlated in time to investigate the stability of the baseline estimate in more detail.

In general, the use of thresholds in classification is not considered best practice as they represent a hard binary choice between two classes, above and below, whereas other techniques can offer a fuzzier probabilistic classification. Processing using hardware circuits imposes considerable constraints on the processing that can be performed and the use of thresholds appeared to be the only tractable design choice. Discrimination of photon detections from noise is the main task that needs to be examined in this light.

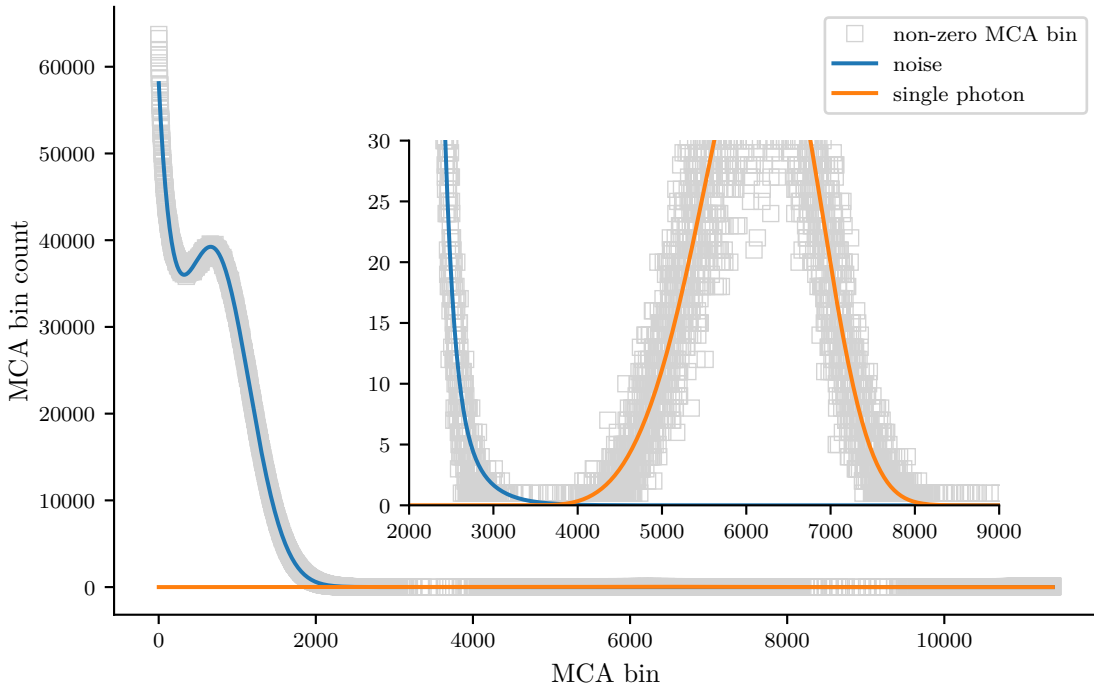


Figure 4.1: The distribution `f_extrema` sequence captured for 1 minute showing the distribution of the maximum value the filtered TES signal (`f`) obtains between baseline (zero) crossings. The inset shows a zoomed in view. On the left is the noise distribution which can be modeled as a mixture of two Weibull distributions (blue line) and on the right is the single photon distribution which can be modeled as a single Weibull distribution (orange line). This information can be used to estimate the probabilities of error in number assignment between the vacuum and single photon term and in turn estimate the single photon loss and dark count (noise) probabilities for a given `pulse_threshold` setting. These probabilities can then be used to complete the POVM, see Equation 3.1. A realtime display could be created that estimates the overlap of the noise distribution and the single photon distribution as an aid in tuning the TES biasing, see Figure 1.2.

In the analysis presented in subsection 3.2.3, the discrimination between signal and noise is achieved using two different thresholds each on different but correlated sequences. A rise

is the detection signal is classified as a photon detection when the filtered TES signal (the `f` sequence) exceeds the `pulse_threshold` setting *and* the maximum value of the slope of `f` (the `s` sequence) exceeds the `slope_threshold` setting during the rise. These threshold settings trade off between efficiency, or loss of a photon detection, and counting noise as photon detection, or dark counts. The settings used to capture the datasets analysed in subsection 3.2.3 favour efficiency and are set into the noise distributions, see Figure 3.3 and Figure 3.4. Table 3.2 contains correlated and uncorrelated counts for the datasets and shows that the dark count rate is roughly 800-900 per hour. Generally dark counts will be assigned a photon number of 1 and loss will be generally of detections that would have been assigned photon number 1. The measurement outcome dependence of these errors degrades the quality of the laser output state estimations. Estimation of the loss of single photon detections is not addressed in my current analysis. Direct accounting of the loss maybe possible using the techniques of correlated photon metrology[Mig08] or with a calibrated attenuator[LGPM15]. The MCA provides an alternative method for estimating the dark count and single photon loss probabilities that I have not analysed in detail.

Figure 4.1 shows the distribution of the `f_extrema` sequence which is the maximum value the filtered TES signal reaches between baseline crossings. The distribution of the TES noise can be modeled as a mixture of two Weibull distributions and the single photon response as another Weibull distribution. The overlap of the noise and single photon distribution can be used to estimate the single photon loss and dark count probabilities in a similar way to Figure 3.8 and be used to add the missing POVM elements in Equation 3.1. The overlap of the noise and single photon distributions depends on the gain of the particular sensor which is subject to fabrication variability and the TES biasing. A realtime display can be constructed using the MCA that would allow the biasing to be adjusted to minimise this overlap. The probabilities of single photon loss and single photon noise are dependent on the threshold settings, which can be used to tune the trade off between dark counts and detection loss.

Another processor feature that can aid in discrimination of signal from noise but has not been analysed, is the dot product measurement returned by the `dot_product` event packet. The dot product module in each channel operates on the same sequence record that would be returned as a trace as specified by the `trace_length`, `trace_stride` and `trace_pre` register settings, see Figure 2.1 and section 2.3. The vector dot product operation is performed on the sequence record and a stored template with the same sequence length then recorded in the `dot_product` field of the event packet. It was shown in [LGM⁺12] that the dot product provides respectable energy discrimination. I expect it also improves discrimination of signal from noise as it incorporates some pulse shape characteristics. By using the average single photon response as a template my expectation, based on these preliminary results, is that a combination of `dot_product` measurement, the `pulse_threshold` and `slope_threshold` settings and perhaps the `rise_time` measurement will significantly improve discrimination of signal from noise.

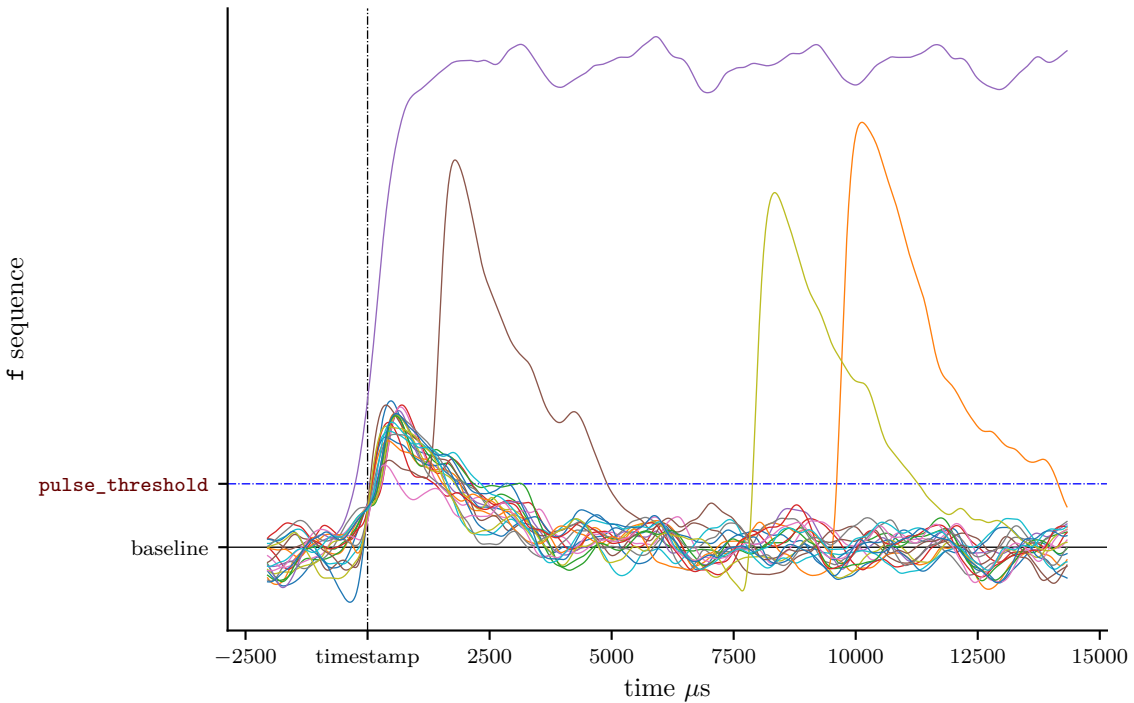


Figure 4.2: Uncorrelated traces captured over 1 minute with `cfd_low` timing. The peaks that are delayed in the traces are due to a noise event triggering the trace capture which was followed by a photon photon event during the time the trace was captured. When capturing only point measurements in a `pulse` event packet two event are seen as separate if the signal falls below `pulse_threshold` between them. In this case, two `pulse` event packets will be returned. For the brown photon event that occurs closest to the timestamp the signal does not fall below the `pulse_threshold` after the noise event triggers the sequence recording. In this case the `pulse` packet will contain two rise records, see Figure 2.1. Multi-rise information has not been used in the analysis presented in this thesis.

It should be noted that the testing and analysis in chapter 3 is performed under non optimal conditions, perhaps even approaching worst case. I choose the sensor that displayed the worst intrinsic gain (due to fabrication variation) to analyse. I biased the sensor “by eye” using an oscilloscope and the live MCA display of the distribution of `f_extrema` signal (without any curve fitting in Figure 4.1) so it is unlikely to be optimally biased. The bandwidth is limited to 1 MHz at the input of the Lecroy amplifier effecting the utility of slope in discriminating signal from noise. The analysis does not use the heralding signal to post select any noise events only to estimate the vacuum count.

4.2 Conclusions

This thesis describes the design development and testing of a hardware circuit library for use with the remarkable Transition Edge Sensor. The library is written in VHDL and a prototype signal processor based on its components is implemented in a Field Programmable Gate Array

for testing. The prototype makes “point” measurements of a TES pulse such as its area, height and length. The goal of the hardware approach is to provide realtime, time and number resolved coincidence counting across multiple channels at the highest rates the sensors can deliver. Existing techniques capture the entire sequence record of a detection pulse and process it in software. Software based approaches allow arbitrarily complex processing which delivers low energy uncertainty but can have potential scalability issues, difficultly delivering information in realtime and trouble capturing long high detection rate records without dropping detection events.

Though testing is preliminary and the analysis is rudimentary the initial results are very encouraging. My optimism is based on the quality of estimates of the laser output state in Figure 3.10, Figure 3.11, Table 3.3. The quality of the estimate is reasonable across the timescales examined. Photon number assignment for all the datasets is based solely on the measurement model derived from the peak3 dataset indicating the characterisation is reasonably stable across different pulse intensities. Least squares and the χ^2 square statistic are not really the most appropriate indicators and more rigorous likelihood based analysis is warranted, this will follow in a peer reviewed publication. Based on the estimate of the likelihood from the least squares minimisation use of the POVM elements (Figure 3.8) does not significantly change the parameter estimates but does improve the likelihood of the fit and therefore the reduced χ^2 . This indicates the estimated POVM elements are reasonable. I believe the increase in variance of the reduced χ^2 with decreasing α seen in Table 3.3 is due to baseline error. In the peak4 dataset most of the electrical pulses that drive the laser result in a detection whereas far less drive pulses produce a detection for the peak1 dataset, see Table 3.2. Under the conditions of the peak1 dataset there are more occasions where the TES cools for 2 or 3 drive pulse periods and this may increase baseline errors as the baseline estimate is based on averaging over longer time scales. Section 4.1 has details of how a second order, per detection baseline estimation can be implemented which would reduce energy uncertainty at low average photon numbers.

The displaced thermal state model for the laser output was introduced during early testing of the prototype. The first data I captured with the processor was produced by a $\sim 830\text{ nm}$ laser diode driven by a 5.6 V 2 ns electrical pulse at 100 khz and under those conditions the displaced thermal model was the best estimate of the laser output state. For the data analysed in this thesis using a $\sim 820\text{ nm}$ diode driven at 100 khz by a 2.6 V 50 ns pulse the thermal character has effectively disappeared and laser output is best modeled using a coherent state. The AIC for both models based on the likelihood estimate from the least squares minimisation does not significantly favour one model over the other. The estimates of \bar{n} the average number of photons in the thermal state before displacement are consistent with $\bar{n} = 0$, see Table 3.4. Further work is required to establish if the thermal nature seen in earlier data is optical or due to measurement error related to baseline estimation. The output estimates should be investigated under different drive repetition rates, pulse widths and voltages. Optical responses of laser

diodes under these drive conditions are not well described in the literature.

Parts of my analysis are still qualitative but I expect that the processor has low enough number uncertainty, as is, for number resolved coincidence counting for the quantum information experiments we have planned with 820 nm photons. There is a clear program of development that will reduce the current energy uncertainty and should make the processor more useful at longer wavelengths where the energy per photon is lower. I don't have any of the standard software techniques implemented in our lab and time pressure prevented me visiting NIST Boulder to see them in action so quantitative comparison of the software and hardware processing approaches is difficult. Ideally a head to head comparison of the two approaches operating on the output from the same sensor should be performed. Many processor features described in ?? are yet to be tested or examined in detail.

The realtime capabilities of hardware processing aid in the setup and optimisation of experiments. My MCA design is capable of operating continuously and without loss at the 250 MHz ADC sampling frequency and opens a novel view on TES signals via capturing the probability distributions of various signal statistics. Use of the MCA may also lead to improved TES biasing procedures (Figure 4.1) and, if the biasing voltages were computer controllable, would enable full automation of TES tuning.

Not described in this thesis is the capture server software that runs on a host computer. Though designed by myself, in parallel with the circuit library, the server software was developed and implemented by fellow PhD student Alexandrina Nickolova. The server captures the packet stream produced by the processor and produces daughter streams for realtime display. This includes the counting of number coincidence patterns. The server software is capable of capturing a full record of the eventstream produced by the processor as a number of indexed files allowing easy access to the data. Data analysed in subsection 3.2.3 was captured in this way. The server streams and the processors registers can be accessed from any network device capable of running Python which allows full automation of data acquisition and control the experimental circuit using python scripts or Jupyter notebooks. I'll leave detailed explanation of the capture server software to Alexandrina's thesis.

There are a number of bugs that need to be addressed, a clear program of improvements to be made, and more rigorous testing and analysis are required but all this is typical of a prototype at this stage of development. Though the design, hardware development, circuit verification, testing and software development for the circuit library was a long and often painful process, I am uncharacteristically pleased with the result.

Bibliography

- [Aka98] Hirotugu Akaike. Information Theory and an Extension of the Maximum Likelihood Principle. In *Selected Papers of Hirotugu Akaike*, pages 199–213. Springer New York, New York, NY, 1998.
- [BA57] D Bohm and Y Aharonov. Discussion of Experimental Proof for the Paradox of Einstein, Rosen, and Podolsky. *Phys. Rev.*, 108(4):1070–1076, November 1957.
- [BA60] D Bohm and Y Aharonov. Further discussion of possible experimental tests for the paradox of Einstein, Podolsky and Rosen. *Il Nuovo Cimento*, 17(6):964–976, September 1960.
- [BAB⁺15] S E Busch, J S Adams, S R Bandler, J A Chervenak, M E Eckart, F M Finkbeiner, D J Fixsen, R L Kelley, C A Kilbourne, S J Lee, S H Moseley, J P Porst, F S Porter, J E Sadleir, and S J Smith. Progress Towards Improved Analysis of TES X-ray Data Using Principal Component Analysis. *Journal of Low Temperature Physics*, 184(1-2):382–388, November 2015.
- [Bel64] John Stewart Bell. On the Einstein Podolsky Rosen paradox. *Physics*, 1(3):195–200, 1964.
- [Bra05] Agata M Branczyk. Quantum control of a single Qubit. Master’s thesis, Physics department, University of Queensland, 2005.
- [CHSH69] John F Clauser, Michael A Horne, Abner Shimony, and Richard A Holt. Proposed Experiment to Test Local Hidden-Variable Theories. *Physical Review Letters*, 23(1):880–884, October 1969.
- [CLFN11] Brice Calkins, Adriana E Lita, Anna E Fox, and Sae Woo Nam. Faster recovery time of a hot-electron transition-edge sensor by use of normal metal heat-sinks. *Applied Physics Letters*, 99(24):241114, 2011.
- [DAB⁺07] D Drung, C Assmann, J Beyer, A Kirste, M Peters, F Ruede, and T Schurig. Highly Sensitive and Easy-to-Use SQUID Sensors. *IEEE Transactions on Applied Superconductivity*, 17(2):699–704, June 2007.

- [DLR77] A P Dempster, N M Laird, and D B Rubin. Maximum Likelihood from Incomplete Data via the EM Algorithm. *Journal of the Royal Statistical Society. Series B (Methodological)*, 39(1):1–38, January 1977.
- [dW00] A T A M de Waele. Pulse-tube refrigerators: principle, recent developments, and prospects. *Physica B: Physics of Condensed Matter*, 280(1):479–482, May 2000.
- [EM] A Einstein and Born M. *The Born-Einstein Letters, 1916-1955*. Friendship, Politics and Physics in Uncertain Times. Times (Macmillan Science).
- [Ens05] Christian Enss. *Cryogenic Particle Detection*. Topics in applied physics. Springer, Berlin, 2005.
- [EPR35] A Einstein, B Podolsky, and N Rosen. Can Quantum-Mechanical Description of Physical Reality Be Considered Complete? *Phys. Rev.*, 47(10):777–780, May 1935.
- [FFCM⁺00] E Figueroa-Feliciano, B Cabrera, A J Miller, S F Powell, T Saab, and A B C Walker. Optimal filter analysis of energy-dependent pulse shapes and its application to TES detectors. *Nuclear Instruments and Methods in Physics Research Section A*, 444(1):453–456, April 2000.
- [FP12] Alessandro Ferraro and Matteo G A Paris. Nonclassicality Criteria from Phase-Space Representations and Information-Theoretical Constraints Are Maximally Inequivalent. *Physical Review Letters*, 108(2):260403, June 2012.
- [GDL⁺10] G G Gillett, R B Dalton, B P Lanyon, M P Almeida, M Barbieri, G J Pryde, J L O’Brien, K J Resch, S D Bartlett, and A G White. Experimental Feedback Control of Quantum Systems Using Weak Measurements. *Phys. Rev. Lett.*, 104(8):080503, February 2010.
- [GHSZ90] Daniel M Greenberger, Michael A Horne, Abner Shimony, and Anton Zeilinger. Bell’s theorem without inequalities. *American Journal of Physics*, 58(12):1131–1143, 1990.
- [GVW⁺15] Marissa Giustina, Marijn A M Versteegh, Sören Wengerowsky, Johannes Handsteiner, Armin Hochrainer, Kevin Phelan, Fabian Steinlechner, Johannes Kofler, Jan-Åke Larsson, Carlos Abellán, Waldimar Amaya, Valerio Pruneri, Morgan W Mitchell, Jörn Beyer, Thomas Gerrits, Adriana E Lita, Lynden K Shalm, Sae Woo Nam, Thomas Scheidl, Rupert Ursin, Bernhard Wittmann, and Anton Zeilinger. Significant-Loophole-Free Test of Bell’s Theorem with Entangled Photons. *Physical Review Letters*, 115(2):250401, December 2015.

- [IH05] K D Irwin and G C Hilton. Transition-Edge Sensors. In Christian Enss, editor, *Cryogenic Particle Detection*, pages 63–150. Springer Berlin Heidelberg, Berlin, Heidelberg, 2005.
- [IHWM98] K D Irwin, G C Hilton, D A Wollman, and John M Martinis. Thermal-response time of superconducting transition-edge microcalorimeters. *Journal of Applied Physics*, 83(8):3978–3985, April 1998.
- [Irw95] K D Irwin. An application of electrothermal feedback for high resolution cryogenic particle detection. *Applied Physics Letters*, 66(15):1998–2000, April 1995.
- [Jar84] Jon P Jarrett. On the Physical Significance of the Locality Conditions in the Bell Arguments. *Noûs*, 18(4):569, November 1984.
- [JNN13] J R Johansson, P D Nation, and Franco Nori. QuTiP 2: A Python framework for the dynamics of open quantum systems. *Computer Physics Communications*, 184(4):1234–1240, April 2013.
- [KLM01] E Knill, R Laflamme, and G J Milburn. A scheme for efficient quantum computation with linear optics. *Nature*, 409(6816):46–52, 2001.
- [Lar98] Jan-Åke Larsson. Bell’s inequality and detector inefficiency. *Physical Review A (Atomic*, 57(5):3304–3308, May 1998.
- [LCP⁺10] A E Lita, B Calkins, L A Pellouchoud, A J Miller, and S Nam. Superconducting transition-edge sensors optimized for high-efficiency photon-number resolving detectors. In Mark A Itzler and Joe C Campbell, editors, *SPIE Defense, Security, and Sensing*, pages 76810D–76810D–10. SPIE, April 2010.
- [Lev44] Kenneth Levenberg. A method for the solution of certain non-linear problems in least squares. *Quarterly of Applied Mathematics*, 2(2):164–168, 1944.
- [LGM⁺12] Zachary H Levine, Thomas Gerrits, Alan L Migdall, Daniel V Samarov, Brice Calkins, Adriana E Lita, and Sae Woo Nam. Algorithm for finding clusters with a known distribution and its application to photon-number resolution using a superconducting transition-edge sensor. *Journal of the Optical Society of America B*, 29(8):2066–, August 2012.
- [LGM⁺14] Zachary H Levine, Boris L Glebov, Alan L Migdall, Thomas Gerrits, Brice Calkins, Adriana E Lita, and Sae Woo Nam. Photon-number uncertainty in a superconducting transition edge sensor beyond resolved-photon-number determination. *Journal of the Optical Society of America B*, 31(10):B20–B24, October 2014.

- [LGPM15] Zachary H Levine, Boris L Glebov, Adam L Pintar, and Alan L Migdall. Absolute calibration of a variable attenuator using few-photon pulses. *Optics Express*, 23(12):16372–, June 2015.
- [Lin00] Mark Anton Lindeman. Microcalorimetry and the transition-edge sensor. *ProQuest Dissertations And Theses; Thesis (Ph.D.)–University of California*, October 2000.
- [LLCT⁺13] Antia Lamas-Linares, Brice Calkins, Nathan A Tomlin, Thomas Gerrits, Adriana E Lita, Jörn Beyer, Richard P Mirin, and Sae Woo Nam. Nanosecond-scale timing jitter for single photon detection in transition edge sensors. *Applied Physics Letters*, 102(2):231117, June 2013.
- [LMN08] Adriana E Lita, Aaron J Miller, and Sae Woo Nam. Counting near-infrared single photons with 95 *Opt. Express*, 16(5):3032–3040, March 2008.
- [LRN⁺05] A E Lita, D Rosenberg, S Nam, A J Miller, D Balzar, L M Kaatz, and R E Schwall. Tuning of Tungsten Thin Film Superconducting Transition Temperature for Fabrication of Photon Number Resolving Detectors. *Applied Superconductivity, IEEE Transactions on*, 15(2):3528–3531, June 2005.
- [McC05] D McCammon. Thermal Equilibrium Calorimeters - An Introduction. *Cryogenic Particle Detection*, 9:1–, 2005.
- [Mig08] Alan Migdall. Correlated-Photon Metrology Without Absolute Standards. *Physics Today*, 52(1):41–46, January 2008.
- [MLC⁺11] Aaron J Miller, Adriana E Lita, Brice Calkins, Igor Vayshenker, Steven M Gruber, and Sae Woo Nam. Compact cryogenic self-aligning fiber-to-detector coupling with losses below one percent. *Opt. Express*, 19(10):9102–9110, May 2011.
- [NCC⁺99] Sae Woo Nam, B Cabrera, P Colling, R M Clarke, E Figueroa-Feficiano, A J Miller, and R W Romani. A new biasing technique for transition edge sensors with electrothermal feedback. *IEEE Transactions on Applied Superconductivity*, 9(2):4209–4212, June 1999.
- [OZ01] Harold Ollivier and Wojciech H Zurek. Quantum Discord: A Measure of the Quantumness of Correlations. *Phys. Rev. Lett.*, 88(1):281, December 2001.
- [Pai79] A Pais. Einstein and the quantum theory. *Review of Modern Physics*, 51(4):863–914, October 1979.
- [SGdA⁺12] Devin H Smith, Geoff Gillett, Marcelo P de Almeida, Cyril Branciard, Alessandro Fedrizzi, Till J Weinhold, Adriana Lita, Brice Calkins, Thomas Gerrits, Howard M

- Wiseman, Sae Woo Nam, and Andrew G White. Conclusive quantum steering with superconducting transition-edge sensors. *Nat Commun*, 3, January 2012.
- [SMSC⁺15] Lynden K Shalm, Evan Meyer-Scott, Bradley G Christensen, Peter Bierhorst, Michael A Wayne, Martin J Stevens, Thomas Gerrits, Scott Glancy, Deny R Hamel, Michael S Allman, Kevin J Coakley, Shellee D Dyer, Carson Hodge, Adriana E Lita, Varun B Verma, Camilla Lambrocco, Edward Tortorici, Alan L Migdall, Yanbao Zhang, Daniel R Kumor, William H Farr, Francesco Marsili, Matthew D Shaw, Jeffrey A Stern, Carlos Abellán, Waldimar Amaya, Valerio Pruneri, Thomas Jennewein, Morgan W Mitchell, Paul G Kwiat, Joshua C Bienfang, Richard P Mirin, Emanuel Knill, and Sae Woo Nam. Strong Loophole-Free Test of Local Realism*. *Physical Review Letters*, 115(2):250402, December 2015.
- [WGR⁺08] Till J Weinhold, Alexei Gilchrist, Kevin J Resch, Andrew C Doherty, Jeremy L O'Brien, Geoffrey J Pryde, and Andrew G White. Understanding photonic quantum-logic gates: The road to fault tolerance. *arXiv.org*, August 2008.
- [WJD07] H M Wiseman, S J Jones, and A C Doherty. Steering, Entanglement, Nonlocality, and the Einstein-Podolsky-Rosen Paradox. *Physical Review Letters*, 98(1):140402, April 2007.